Global Biogeochemical Cycles®

RESEARCH ARTICLE
10.1029/2025GB008856

Drivers of Benthic Iron Fluxes and the Pore-Water Iron Isotopic Signature in Surface Sediments of South Georgia Fjords, Sub-Antarctica

Berenice Ebner[1,2], Susann Henkel[1,3], Peter Kraal[4], Daniel Müller[1,2], Male Köster[1], Michael Staubwasser[5], Katja Laufer-Meiser[6], Laura Kattein[1,2], Walter Geibert[1], and Sabine Kasten[1,2,3]

[1]Alfred Wegener Institute Helmholtz Centre for Polar and Marine Research, Bremerhaven, Germany, [2]University of Bremen, Faculty of Geosciences, Bremen, Germany, [3]MARUM-Center for Marine Environmental Sciences, University of Bremen, Bremen, Germany, [4]Department of Ocean Systems, Royal Netherlands Institute for Sea Research, 't Horntje, The Netherlands, [5]Institute of Geology and Mineralogy, University of Cologne, Cologne, Germany, [6]GEOMAR-Helmholtz Centre for Ocean Research Kiel, Kiel, Germany

Abstract Benthic iron (Fe) fluxes from coastal sediments support phytoplankton blooms downstream of subpolar islands. We combine solid-phase and pore-water geochemical data, including its iron isotopic signature ($\delta^{56}Fe_{aq}$), to identify the main drivers of benthic Fe fluxes from sub-Antarctic fjord and shelf sediments of South Georgia, and to evaluate the potential of $\delta^{56}Fe_{aq}$ as a proxy for benthic Fe fluxes. A high accumulation rate of total organic carbon compresses the redox zonation in the near-surface sediment column and controls benthic Fe efflux. Sites with low diffusive Fe fluxes show a broad $\delta^{56}Fe_{aq}$ range close to the sediment-water interface (-3.94 ± 0.14‰ to -0.98 ± 0.11‰), while sites with high benthic Fe fluxes exhibit a slightly narrower range (-3.14 ± 0.02‰ and -1.64 ± 0.06‰). The broader isotopic range in low benthic Fe flux settings reflects the diverse processes that entail low net benthic Fe fluxes into the bottom water. Low- and high rates of microbial iron reduction may result in similar Fe isotope composition of diffusive benthic Fe efflux, if the latter is combined with high rates of Fe removal from pore-water by iron sulfide formation. A narrow range of $\delta^{56}Fe_{aq}$ within the oxic redox zone appears to be a recurrent feature at sites of high benthic Fe fluxes, but we recommend accounting for all early diagenetic Fe cycling processes and the depositional regime when interpreting low $\delta^{56}Fe_{aq}$ values in the near bottom water.

Plain Language Summary Iron is an essential but in the Southern Ocean often limited nutrient that algae need to grow. In the Southern Ocean, input from ocean island archipelagos is the main iron supplying source in island influenced regimes. Shallow marine sediments surrounding these islands are an important contributor because microbial organic matter decomposition therein can effectively recycle iron into the water column in a more soluble form. This process, microbial iron reduction, is known to leave a fingerprint in the iron isotopic composition that could be used to identify and potentially quantify its contribution. We analyzed sediment and pore-water inside two fjords in South Georgia and found that the dynamic depositional environment of glaciated fjords presents challenges for using stable iron isotopes to identify recycled sedimentary iron fluxes, particularly when iron sulfide formation lowers benthic iron flux and imprints an isotopic fingerprint similar to microbial iron reduction.

Key Points:

- Dynamic heterogeneous depositional conditions prevail in subpolar fjords with marine terminating glaciers affecting benthic iron efflux
- Total organic carbon accumulation rates control benthic iron fluxes into the bottom water
- Sites with low benthic iron fluxes into bottom water show a broad range of pore-water iron isotopic values

Supporting Information:

Supporting Information may be found in the online version of this article.

Correspondence to:

B. Ebner and S. Henkel,
berenice.ebner@awi.de;
susann.henkel@awi.de

Citation:

Ebner, B., Henkel, S., Kraal, P., Müller, D., Köster, M., Staubwasser, M., et al. (2026). Drivers of benthic iron fluxes and the Pore-water iron isotopic signature in surface sediments of South Georgia fjords, sub-Antarctica. *Global Biogeochemical Cycles*, *40*, e2025GB008856. https://doi.org/10.1029/2025GB008856

Received 4 SEP 2025
Accepted 20 MAR 2026

Author Contributions:

Conceptualization: Berenice Ebner, Susann Henkel, Sabine Kasten
Data curation: Berenice Ebner, Daniel Müller, Male Köster, Laura Kattein
Formal analysis: Berenice Ebner, Daniel Müller
Funding acquisition: Susann Henkel, Sabine Kasten
Investigation: Berenice Ebner, Male Köster, Michael Staubwasser, Katja Laufer-Meiser, Laura Kattein, Sabine Kasten
Methodology: Berenice Ebner, Susann Henkel, Peter Kraal, Daniel Müller, Male Köster, Walter Geibert, Sabine Kasten

1. Introduction

The Southern Ocean (SO) hosts about 20% of the global marine primary production (Behrenfeld & Falkowski, 1997). Marine primary productivity has been shown to depend on the availability of the micronutrient iron (Fe), particularly in high-nutrient low-chlorophyll regions (e.g., Boyd & Ellwood, 2010). Iron supply to the open ocean photic zone originates from the natural fertilization of deeper waters with Fe over the shelf and upper slope surrounding ocean island plateaus (e.g., Blain et al., 2007; Stimpfle et al., 2026). Ocean islands provide a significant influx of terrestrial Fe, which occurs by direct discharge from glaciers. This source comprises a particulate component from eroded rock flour (Raiswell et al., 2006) and a dissolved component from a subglacial outflow (Wadham et al., 2013). In addition, there is a contribution by benthic recycling of detrital Fe from island surface runoff as well as from subglacial erosion (Nielsdóttir et al., 2012). In island-influenced regions such as South Georgia (SG), other potential Fe sources to the open ocean such as atmospheric dust (Jickells et al., 2005),

Resources: Michael Staubwasser, Walter Geibert, Sabine Kasten
Supervision: Susann Henkel, Sabine Kasten
Visualization: Berenice Ebner, Peter Kraal

(sub)marine groundwater discharge (Burnett et al., 2003) and hydrothermal input (Klar, James, et al., 2017) are thought to play only a subordinate role. However, benthic efflux rates can be substantial in the subglacial islands coastal environment (Monien et al., 2014). Recent studies on sediments from the eastern shelf of the Antarctic Peninsula to the West of the South Orkney Islands showed that higher organic matter burial fluxes enhance microbial Fe reduction, thereby enhancing Fe efflux to the bottom water (BW) (Baloza et al., 2022, 2023). However, over the deeper shelf and slope regions, Fe turnover within the mixed layer's biological recycling loop increasingly outpaces vertical benthic upward diffusion (Schlosser et al., 2018).

Iron fluxes to the SO are likely to change under global warming and not all potential Fe sources are anticipated to contribute continuously or respond equally to environmental changes (Dale et al., 2015; Death et al., 2014; Tagliabue et al., 2019). In particular, continental shelf and slope sediments are recognized as a substantial contributor of dissolved Fe (dFe) to the global ocean Fe budget (Elrod et al., 2004; Klar, Homoky, et al., 2017). A recent study by van de Velde et al. (2023) estimated the total global diffusive Fe flux from modern marine shelf sediments to be 4,200 ± 2100 Gg yr^{-1} (area: 27.12 × 10^6 km^2; maximum water depth 200 m according to Menard & Smith, 1966), while Monien et al. (2014) estimated a diffusive Fe flux from the Antarctic shelf to the SO ranging from 6.9 to 790 Gg yr^{-1} (area: 2.4 × 10^6 km^2; maximum water depth 500 m). Because of the low temporal and spatial resolution of available data on benthic Fe fluxes, the quantification of global Fe fluxes from shelf sediments is currently poorly constrained (Dale et al., 2015). Despite their potential importance, both the magnitude of benthic Fe fluxes and the processes controlling them remain highly uncertain, motivating the use of complementary approaches to better constrain benthic Fe efflux.

In this context, it has also been suggested that the isotopic signature of pore-water Fe in surface sediments, which it acquires during microbial Fe reduction, imprints itself on the Fe isotope composition ($\delta^{56}Fe_{aq}$) of open ocean water (Crosby et al., 2007; John et al., 2012). Analysis of the pore-water $\delta^{56}Fe_{aq}$ composition is commonly used to discriminate between the different redox-driven early diagenetic processes that result in accumulation of dFe (Henkel et al., 2018, 2025; Johnson & Beard, 2005; Köster et al., 2023; Sivan et al., 2011). Several studies proposed that $\delta^{56}Fe_{aq}$ in the open ocean reflects specific Fe isotope fractionation processes, which are attributed to different Fe sources of input (Conway & John, 2014; John et al., 2012, 2018; Klar, Homoky, et al., 2017; Lacan et al., 2008; Sieber et al., 2021; Tian et al., 2023). Microbial Fe reduction, which can lead to high dFe concentrations in subglacial waters as well as marine sediments, has been shown to enrich the light isotope ^{54}Fe in the dissolved pool with a fractionation factor $\Delta^{56}Fe_{Fe(III)reac-Fe(II)aq} = 2.95 \pm 0.68‰$ (Crosby et al., 2007; Henkel et al., 2016, 2018; Severmann et al., 2010; Stevenson et al., 2017). Competing redox reactions, for example, microbial Fe (oxyhydr)oxide reduction and Fe sulfide formation with different effects on the pore-water $\delta^{56}Fe_{aq}$ composition (e.g.,; Henkel et al., 2025; Severmann et al., 2010), and variable deposition rates of organic matter and reactive Fe (oxyhydr)oxides may lead to a locally variable range of $\delta^{56}Fe_{aq}$ values in near-surface pore-water and benthic Fe efflux (Henkel et al., 2018; Severmann et al., 2010). When non-reductive dissolution dominates, $\delta^{56}Fe_{aq}$ values reflect the local rock and sediment composition (Homoky et al., 2013; Radic et al., 2011), which are generally close to zero (Beard et al., 2003). At any given location, dFe may be the product of a multitude of biotic and abiotic reactions. Thus, the local marine $\delta^{56}Fe_{aq}$ signature represents the weighted sum of all processes of Fe isotope fractionation (Fitzsimmons & Conway, 2023). Many marine Fe isotope studies address either water column or sedimentary processes, while the coupling across the sediment-water interface (SWI) and the depositional regime remains poorly constrained, yet essential for interpreting water column Fe isotope signatures.

As global warming causes widespread and rapid glacial retreat on SO islands, Fe fertilization from these islands is expected to increase (Tagliabue et al., 2019). At the same time, the factors controlling benthic Fe fluxes and the extent to which pore-water $\delta^{56}Fe_{aq}$ values can be linked to the magnitude of benthic dissolved Fe release are unresolved. Furthermore, integrative studies of the depositional conditions and sediment diagenesis are required to gain a better understanding of benthic sediments as an Fe source in the open ocean. We assess the role of islands in fertilizing the ocean by (a) quantifying the benthic Fe flux rates in surface sediments of fjords and shelf areas of South Georgia, (b) identifying the dominant drivers controlling the magnitude of these benthic Fe fluxes, and (c) evaluating whether the near-surface pore-water $\delta^{56}Fe_{aq}$ signature exhibits a relationship with benthic Fe fluxes to serve as a basis for using water-column $\delta^{56}Fe_{aq}$ values as a proxy for benthic Fe release.

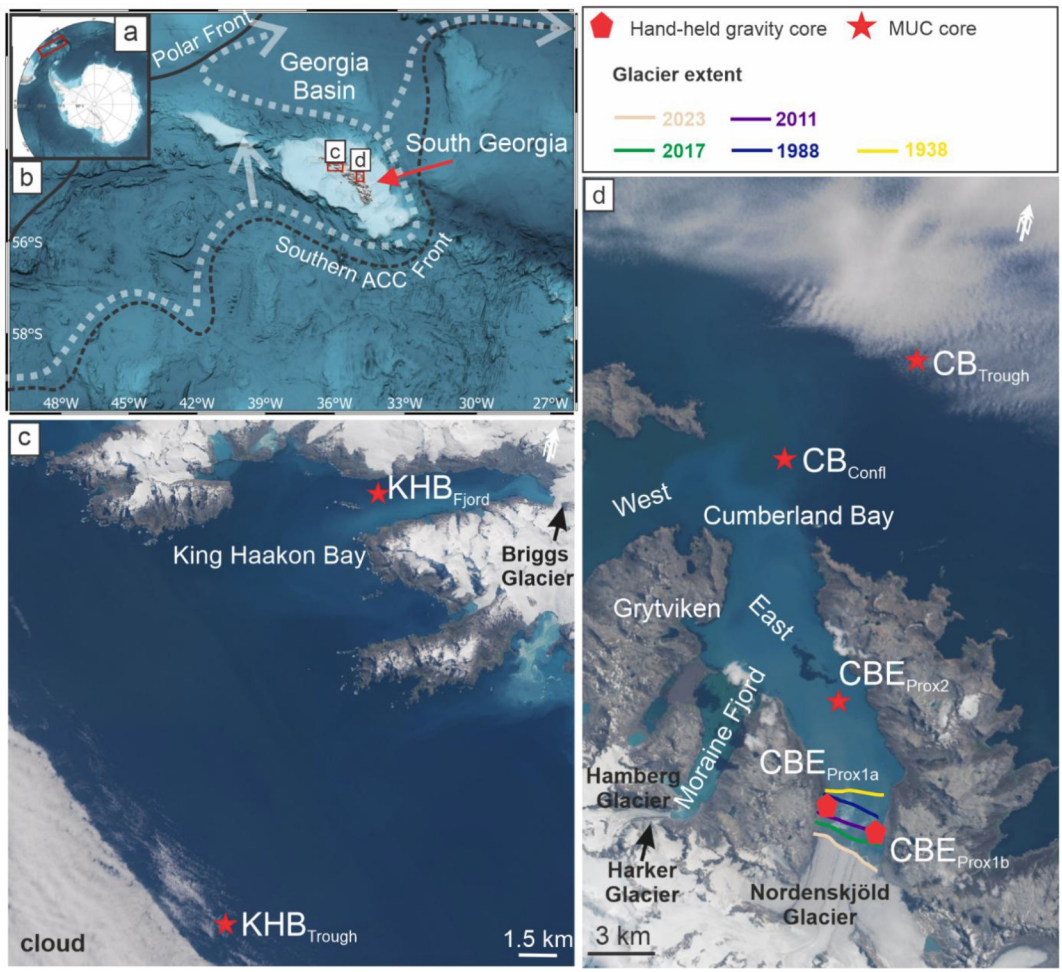

Figure 1. (a) Bathymetric map of the Southern Ocean based on Dorschel et al. (2022). Red rectangle: study area South Georgia. (b) Study area (red arrow) with the Polar Front and the Southern Antarctic Circumpolar Current Front (Meredith et al., 2003). White arrows schematically show the circulation in the upper layer of the ocean (0–500 m) after Matano et al. (2020). (c) Location of the coring sites at King Haakon Bay (KHB): King Haakon Bay Fjord (KHB_{Fjord}) and King Haakon Bay Trough (KHB_{Trough}). (d) Location of the coring sites at Cumberland Bay East (CBE_{Prox1a}, CBE_{Prox1b}, and CBE_{Prox2} (subscripts: proximal 1 and 2), Cumberland Bay Confluence (CB_{Confl}); Cumberland Bay Trough (CB_{Trough}). The retreat of the Nordenskjöld Glacier (colored lines) is shown after Tichit et al. (2024). Coring devices are indicated by symbols (red star: multicorer; red pentagon: UWITEC hand-held gravity corer). Satellite image: CBE: Sentinel-2 L1C taken 01/2023; KHB taken 11/2021.

1.1. Study Area

South Georgia (54°S, 36°W, ~3,500 km^2) is a sub-Antarctic archipelago located between the Antarctic Peninsula and South America at the NE bound of the Scotia Sea (Figure 1a). The Antarctic Circumpolar Current (ACC) flows from west to east around the Antarctic Peninsula driven by westerly winds (Orsi et al., 1995). The southern ACC front (SACCF) loops around SG anticyclonically (Figure 1b) (Meredith et al., 2003; Zanker et al., 2024). Large phytoplankton blooms occur NW (downstream) of the island in the Georgia Basin (Borrione & Schlitzer, 2013), likely fueled in part by wind-driven Ekman Buoyancy Flux, which can supply significant amounts of Fe from subsurface water to the mixed layer (Mole et al., 2025). In this study, we focus on two fjords: Cumberland Bay (CB), specifically its eastern branch (CBE) (Figure 1d), located in the NE, and King Haakon Bay (KHB) (Figure 1c) in the SW of SG. The CBE fjord is ~15 km long, 3–5 km wide and up to 270 m deep. The 6-km-long tributary fjord, Moraine Fjord (MF), merges with the CBE to the southwest (Figure 1d) (Hodgson et al., 2014). The Nordenskjöld Glacier (catchment area 135.5 km^2) discharges into the CBE, and two, considerably smaller, glaciers discharge into the MF (Bentley et al., 2007; Gordon et al., 2008; Hodgson et al., 2014). In Grytviken at

Table 1
Station Information Including Coordinates, Water Depth, and Distance to the Tidewater Glaciers Nordenskjöld Glacier (Cumberland Bay East) and Briggs Glacier (King Haakon Bay)

Station	Ice-	Station ID	Trivial name	Location		Water depth (m)	Distance to tidewater glacier (km)
				Latitude (S)	Longitude (W)		
Cumberland Bay (CB) East (CBE)	distal	PS133/2_50-6	CB_{Trough}	54°03.920′	36°08.554′	270.4	44.7
		PS133/2_42-8	CB_{Confl}	54°12.491′	36°26.599′	264.6	19.7
	proximal	PS133/2_36-1	CBE_{Prox1a}	54°21.144′	36°22.017′	144.4	1.3
		PS133/2_36-2	CBE_{Prox1b}	54°21.138′	036°22.020′	144.6	1.3
		PS133/2_35-6	CBE_{Prox2}	54°20.745′	36°22.705′	160.4	2.5
King Haakon Bay (KHB)	distal	PS133/2_17-11	KHB_{Trough}	54°24.067′	37°34.074′	344.1	39.8
	distal	PS133/2_23-9	KHB_{Fjord}	54°09.573′	37°23.181′	153.8	10.5

Note. CB_{Trough} = Cumberland Bay Trough, CB_{Confl} = Cumberland Bay Confluence, CBE_{Prox1a} = Cumberland Bay East (proximal 1a), CBE_{Prox1b} = Cumberland Bay East (proximal 1b), CBE_{Prox2} = Cumberland Bay East (proximal 2), KHB_{Trough} = King Haakon Bay Trough, KHB_{Fjord} = King Haakon Bay Fjord.

CB, a whaling station was operated from 1904 to 1965, potentially affecting the biogeochemistry in the fjord as exploited animal carcasses were discarded into the bay after oil extraction and collection of whale and seal blubber (Smith, 2018). KHB, the narrowest and with ∼13 km the longest fjord of SG, is 1–3 km wide and up to 160 m deep. At the fjord head, the Briggs Glacier terminates in the fjord (Figure 1c), and numerous smaller tributary glaciers enter the fjord at the southern shore. The King Haakon Trough is located on the outer shelf (Hodgson et al., 2014; Lešić et al., 2024) and was formed by glacial erosion (Streuff et al., 2024). The predominant lithology of the island (including the KHB and MF catchment) comprises cretaceous andesitic volcanoclastic greywackes and shales (Cumberland Bay Formation) and the CBE hinterland is characterized by the Sandebugten Formation comprising quartz-rich sandstones and shales (Curtis, 2011; Mair, 1981).

Numerous studies on sediments have been conducted to investigate the geochemical characteristics at various sites around SG (Berg et al., 2021; Schnakenberg et al., 2021; Wunder et al., 2021). High dissolved methane concentrations were found in the water column of the CBE ("Grytviken Flare") and at the confluence zone, where the western and eastern branch of CB fjord merge ("Cumberland Bay Flare") (Geprägs et al., 2016; Römer et al., 2014). Active methane seeps have been detected as flares in the water column by means of hydroacoustic surveys during research vessel RV Polarstern expeditions ANT-XXIX/4 (Bohrmann, 2013) and PS133/2 (Kasten, 2023). Studies have demonstrated that active ebullition of methane gas might increase benthic fluxes via bubble-induced mixing (Haeckel et al., 2007). However, the sites investigated in this study are at least 800 m away from known active methane seeps (Table S8 in Supporting Information S1) (personal communication Miriam Römer). We therefore consider the effect to be negligible.

2. Material and Methods

2.1. Pore-Water and Sediment Sampling

The RV Polarstern expedition PS133/2 "Island Impact" was carried out in the South Georgia area of the Southern Ocean during the austral summer in November and December 2022 (Kasten, 2023). During this expedition, samples were collected on a transect in CBE (Figure 1d) and in the KHB Fjord (Figure 1c). The sediment cores from CBE were classified, with regard to the distance to the (marine-terminating) glacier terminus, into (a) ice-proximal and (b) ice-distal sites, whereas both KHB sites were classified as ice-distal (Table 1). Due to the inaccessibility by RV Polarstern and time-limitations, we were unable to collect samples from the head of the KHB Fjord. Undisturbed surface sediments were retrieved by a multiple corer (MUC) from board of the RV Polarstern and a hand-held- gravity corer (UWITEC) on board of a zodiac. At each sampling site except site CBE_{Prox1a}, two MUC cores (MUC 1 and 2) were used to extract pore-water for the analysis of phosphate (PO_4^{3-}), sulfate (SO_4^{2-}) alkalinity, hydrogen sulfide (H_2S), dissolved inorganic carbon (DIC) and dissolved cations (e.g., Mn and Fe). MUC 2 was also used for the analysis of stable Fe isotopes ($\delta^{56}Fe_{aq}$). After core retrieval, MUCs 1 and 2 were sliced into 1–2 cm segments and placed into 50 ml centrifuge tubes. The pore-water was subsequently sampled using a 10 cm rhizon with an average nominal pore size of 0.15 µm (Seeberg-Elverfeldt et al., 2005). After that, the remaining sediment samples were flushed with N_2 to avoid oxidation and stored at −20°C. Sub-

samples of 1 ml pore-water were acidified with double-distilled HCl for major and minor cation analyses. Samples for H_2S analyses were fixed with 5% Zn-acetate. Samples for DIC were treated with 10 µl $HgCl_2$ and stored in vials without headspace. All pore-water aliquots were stored at 4°C. The sediment of MUC 2 was used for 0.5 M HCl extractions of the sediments to determine reactive Fe contents (Laufer et al., 2020). A third MUC core was used for ex situ oxygen measurements and was subsequently sliced for $^{210}Pb_{xs}$ analysis to determine sedimentation and mass accumulation rates. A fourth MUC and another core collected with a hand-held gravity corer (CBE_{Prox1b}) were used to determine sulfate reduction rates (SRR). MUC 4 was subsampled with 2.5 cm diameter acrylic core-liners. The core-liners had pre-drilled holes that were sealed with polyurethane-based elastic sealant (Sikaflex®-11FC+, Sika), through which 50 kBq of carrier-free ^{35}S–SO_4^{2-} were injected at 1 cm depth intervals. For the hand-held gravity core at CBE_{Prox1b}, it was impossible to take a separate core and SRR were measured after syringe incubations: a 1 cm^3 sample was taken with a glass syringe while slicing the core in a glove bag (N_2 atmosphere). The syringe was closed with a butyl stopper and 50 kBq of carrier-free ^{35}S–SO_4^{2-} was injected into each syringe. Syringes (CBE_{Prox1b}) and whole cores (all other stations) were incubated for 14–18 hr at near in situ temperature. The incubations were stopped by slicing the cores into 1 cm segments and adding the sediment to Falcon tubes containing 10 ml of 20% Zn acetate. The sediment from each syringe was accordingly treated to stop the incubation. Samples were stored frozen at −20°C until further processing at the GEOMAR Helmholtz Center for Ocean Research Kiel.

2.2. Pore-Water Analyses

The oxygen concentrations in the BW of the MUC cores were determined by iodometric titration after Winkler (1888). Ex-situ oxygen measurements were conducted in a cool room (+4°C) on board of the vessel using fiber-optical retractable needle-type oxygen microsensors (OXR50-HS; HS: High Speed; diameter: 50 µm; Pyroscience, Germany). Phosphate (PO_4^{3-}) was analyzed on board in an aliquot of filtered pore-water using a QuAAtro39 Continuous Segmented Flow Analyzer (SEAL Analytical). Measurements of the certified reference materials KANSO Lot.CO-0730 and KANSO Lot.CL-1229 resulted in recoveries of 92.9 ± 15.2% (2SD, $n = 16$) and 100.6 ± 13.4% (2SD, $n = 16$), respectively. Alkalinity was determined by titration with HCl (50 or 100 mM) using a digital burette (Metrohm 775 Dosimat) to a pH of ∼3.9 and the calculation was made according to Grasshoff et al. (1999). For each set of samples, the certified seawater standard IAPSO (certified alkalinity of 2.325 mM) was titrated three times. The alkalinity of pore-water samples was then corrected for the deviation of the measured mean value from the certified value. In order to approximate the dFe concentrations for the sampling for $\delta^{56}Fe_{aq}$, dFe was determined on board using the ferrozine method (Stookey, 1970). The dissolved Fe (dFe), but also Mn (dMn) concentrations were further determined by Inductively Coupled Plasma Optical Emission Spectrometry (ICP-OES) using a Thermo Scientific iCAP 74B00 at the Alfred Wegener Institute Helmholtz Center for Polar and Marine Research (AWI) in Bremerhaven. Internal yttrium standard was applied to correct for variations in the ionic strength of the samples. The limits of detection and quantification (LOQ) were calculated according to Küster and Thiel (1985): for dissolved Fe, those were 0.54 and 2.33 µM and for dMn 0.36 and 2.37 µM. Recoveries of a measured Fe- and Mn-spiked IAPSO were 104.9 ± 4.5% for dFe ($n = 9$) and 103.8 ± 3.1% for dMn ($n = 9$). Hydrogen sulfide was determined via the methylene blue method after Cline (1969). Sulfate concentrations were measured using the Metrohm 930 Compact IC Flex with a Metrosep A Supp 5 150/4.0 chromatography column. The reference material IAPSO and a lab internal standard (anion multielement standard) resulted in recoveries of 99.5 ± 4.2% (2SD, $n = 40$) and 95.6 ± 2.4% (2SD, $n = 40$), respectively. DIC concentrations were measured in the laboratory at AWI using a QuAAtro39 Continuous Segmented Flow Analyzer (SEAL Analytical). A certified seawater CO_2 reference material (Dickson, 2010; Stoll et al., 2001) revealed a recovery of 107.3 ± 10% (2SD, $n = 20$).

Pore-water samples for $\delta^{56}Fe_{aq}$ analyses ($n = 34$) were processed at the AWI. Ten ml of the pore-water was evaporated in an open system and redissolved in 5 M HCl +0.001% v/v suprapur® H_2O_2. Subsequently, the samples were purified by anion exchange column chromatography using the AG-MP1 resin (Homoky et al., 2013; Köster et al., 2023). Column calibration using an in-house multielement standard prepared according to maximal cation concentrations expected in pore-water ensured that columns were not overloaded and that Fe was properly separated from all other elements (Figure S1 in Supporting Information S1). In addition, to fully exclude Fe loss during column separation, the distinct splits from sample loading and the elution of matrix elements were collected and measured by ICP-mass spectrometry (ICP-MS Element 2, Thermo Scientific). For all samples, the loss of dFe during the processing was <3%. The isotope reference material AC-E, a granite from Alisa Craig

Island, Scotland, for which solutions were prepared to match pore-water concentrations, was processed with each batch of pore-water samples (Köster et al., 2023). After processing, the measured AC-E values were 0.33 ± 0.05‰ (2SD, $n = 3$) with a target value of 0.32 ± 0.01‰ (2SD; Craddock & Dauphas, 2011). After column chromatography, sub-samples of pore-water solutions were matched to 0.2 ppm for $\delta^{56}Fe_{aq}$ analysis on a Neptune plus Multicollector (MC)- ICPMS at the University of Cologne, Germany. The Neptune plus was equipped with an ESI Apex-IR desolvator and nickel cones. ^{53}Cr and ^{60}Ni were measured to monitor interferences of ^{54}Cr on ^{54}Fe and ^{58}Ni on ^{58}Fe, and the data were corrected accordingly. The sample-standard bracketing method was applied using the reference standard IRMM-524B (Köster et al., 2023; Schoenberg & Von Blanckenburg, 2005). Data are reported as

$$\delta^{56}\mathrm{Fe}\,[‰] = \left[\left({}^{56}\mathrm{Fe}/{}^{54}\mathrm{Fe}_{\mathrm{sample}}\right)/\left({}^{56}\mathrm{Fe}/{}^{54}\mathrm{Fe}_{\mathrm{IRMM-524B}}\right) - 1\right] * 1000$$

The uncertainty of individual samples is given as the twofold standard deviation (2SD) of replicate measurements ($n = 68$). The reproducibility and external precision of the measurements were checked by analysis of the standard material Johnson and Matthey, Fe Puratronic wire (JM), which was run as a sample following each set of six pore-water samples. Measured $\delta^{56}Fe$ values for the JM were 0.43 ± 0.04‰ (2SD, $n = 20$) and aligned with published data (0.42 ± 0.05‰, 2SD; Schoenberg & Von Blanckenburg, 2005). Processing replicates ($n = 5$) were within the 2SD of the replicate measurements of individual samples.

2.3. Calculation of Diffusive Iron Fluxes Toward the Oxic Layer and Across the Sediment-Water Interface

We calculated both the diffusive fluxes of dFe toward the oxic layer ($J_{\mathrm{dFe\ towards\ oxic\ layer}}$) and across the sediment-water interface (SWI) ($J_{\mathrm{dFe\ across\ SWI}}$). The $J_{\mathrm{dFe\ towards\ oxic\ layer}}$ (mol $m^{-2}d^{-1}$) was calculated using Fick's first law of diffusion:

$$J_{\mathrm{dFe\ \ towards\ oxic\ layer}} = -\varphi D_s \frac{dC}{dx} \quad (1)$$

where D_s is the diffusion coefficient in the sediment ($m^2\ d^{-1}$), dC/dx represents the concentration gradient and ϕ is the porosity averaged over the respective intervals. The diffusion coefficient in the sediment is:

$$D_s = \frac{D^{\mathrm{SW}}}{\theta^2} \quad (2)$$

where θ is the tortuosity:

$$\theta^2 = 1 - \ln(\varphi^2) \quad (3)$$

and D^{SW} is the diffusion coefficient in a free solution of seawater (Boudreau, 1997). For our calculations, we used the D^{SW} for dFe at 0°, which is $3.15*10^{-10}$ ($m^2\ d^{-1}$). For the concentration gradient we used measured dFe values below the oxic zone, as these values are more robust (Figure S2 in Supporting Information S1) and excluded values that might have been affected by oxidation processes. The $J_{\mathrm{dFe\ across\ SWI}}$ (mol $m^{-2}d^{-1}$) was calculated after Boudreau and Scott (1978):

$$J_{\mathrm{dFe\ \ across\ SWI}} = \frac{\varphi(D_s k_1)^{0.5}\, c_P}{\sinh\left[\left(\frac{k_1}{D_s}\right)^{0.5} L\right]} \quad (4)$$

where ϕ is the porosity at the core top (0–0.01 m), k_1 is the first order rate constant for Fe oxidation in seawater (s^{-1}), c_p represents the pore-water concentration of dFe (mol m^{-3}) at the bottom of the oxygenated sediment surface layer and L is the thickness of the oxic layer (m). For c_p we used values relative to the lower boundary of the oxic zone, unaffected by the processes within the oxic zone (Figure S2 in Supporting Information S1). To derive k_1, we used the following equations (Millero & Izaguirre, 1986):

$$k_1 = k[O_2][OH^-]^2 \quad (5)$$

$$\log k = 21.56 - \frac{1545}{T} - 3.29I^{0.5} + 1.52I \quad (6)$$

where I is the ionic strength of seawater (0.723), T is the temperature in Kelvin, and the first-order rate constant k_1 is a function of BW O_2 and OH^- concentrations (Raiswell & Anderson, 2005). For the calculations, a pKw of 14.3 at 0°C is used (Millero, 2001). The pore-water profiles of alkalinity and DIC were used to calculate the corresponding pH for all sites using the *R* package seacarb (Gattuso et al., 2021) with $T = 0$°C and a salinity of 34 psu and the dissociation constants of Roy et al. (1993), which are valid over the full temperature and salinity range covered by our data set. The pH values were reported on the total scale. Varying assumed salinities between 20 and 35, reflecting potential freshwater influence in glaciated fjord systems, change the calculated pH by ≤0.1 units. Pore-water chloride concentrations indicate a mean value of 514 ± 19.5 mM (1 SD) across all cores. This corresponds to only moderate freshwater dilution, while the glacier-proximal (CBE_{Prox1a}) minimum of 456 mM (at 19.5 cm) represents an outlier. Importantly, this observed range is within the salinity interval tested in the sensitivity analysis and therefore cannot account for the observed pH patterns. In our data set, dissolved sulfide (H_2S) is below the analytical detection limit in bottom waters. Sensitivity calculations assuming sulfide concentrations at the detection limit show no observable effect on the calculated pH. The contribution of sulfide alkalinity is therefore negligible. For deeper sediment intervals, where H_2S is present, sulfide alkalinity was accounted for using the carbfull function in the seacarb *R* package (Gattuso et al., 2021). Uncertainties in calculated pH values were quantified using Monte Carlo simulations ($n = 1000$), where analytical uncertainties in DIC and alkalinity were propagated through the calculations. All parameters involved in the calculations are given in Table S1 of Supporting Information S1. In order to assess the variability of the flux calculations, $J_{dFe\ towards\ oxic\ layer}$ and $J_{dFe\ across\ SWI}$ were calculated for both MUC 1 and MUC 2 (Table S2 in Supporting Information S1). The J_{dFe} shown in the following are those based on ICP-OES data from MUC 2. For comparability, we used the same core as we used to obtain the $\delta^{56}Fe_{aq}$ data. We note that the equation of Boudreau and Scott (1978) to calculate the $J_{dFe\ across\ SWI}$ neglects bioirrigation, bioturbation and ligand stabilization, contributing to the large uncertainty of the calculated fluxes. The uncertainty estimates of the $J_{dFe\ across\ SWI}$ reflect the variability of fluxes calculated over different depth intervals close to the SWI, as this approach captures the sensitivity of the $J_{dFe\ across\ SWI}$ calculations to the depth interval rather than analytical measurement uncertainty. The uncertainty of the Fe flux toward the oxic layer was quantified using error propagation.

2.4. Solid Phase Analyses

Wet sediment equivalent to ∼50 mg dry weight was used to determine reactive Fe phases according to extractions after Laufer et al. (2020). The extraction with 0.5 M HCl (1 hr at room temperature) dissolves poorly crystalline $Fe(III)_s$, which is hereafter called "reactive" Fe based on the definition by Heron et al. (1994) and $Fe(II)_s$ bound in acid volatile sulfide (AVS) and Fe carbonates. In a recent study on synthetic ferrihydrite and lepidocrocite it was found that during 0.5 M HCl extractions no lepidocrocite is extracted (Kraal et al., 2022), hence poorly crystalline $Fe(III)_s$ (0.5 M HCl extractable $Fe(III)_s$) is assumed to be mainly bound in ferric oxyhydroxides (FeOOH). We processed sediment surface samples down to the dFe concentration maximum at the respective sites. The $Fe(II)_s$ and total Fe concentrations in the extracts were determined using the ferrozine method (Stookey, 1970). For the determination of the total Fe concentration hydroxylamine-hydrochloride (HAHCl) was used to reduce all dissolved $Fe(III)_s$ to $Fe(II)_s$. $Fe(III)_s$ was then calculated from the difference between total Fe and $Fe(II)_s$ concentrations. The in-house standard HE443-077-cc, which was collected from a core catcher of a gravity core deployment in the North Sea (Henkel et al., 2016), ($n = 6$) resulted in reactive Fe contents of which 0.41 ± 0.07 wt.% were $Fe(II)_s$ and 0.34 ± 0.07 wt.% were $Fe(III)_s$. These values are in the range of Fe contents previously measured at AWI for the same material ($Fe(II)_{0.5\ M\ HCl} = 0.37 \pm 0.09$ wt.%; $Fe(III)_{0.5\ M\ HCl} = 0.36 \pm 0.09$ wt.%; $n = 12$). Duplicate measurements of samples from SG ($n = 4$) reveal a difference between two values below 5%.

To determine the porosity, samples were weighed, freeze-dried, and weighed again to calculate the mass fraction, the dry mass, and water content. Subsequently, the porosity was calculated assuming a sediment bulk density of 2.67 g cm^{-3} (e.g., Breitzke, 2006). The freeze-dried samples were used to determine the total organic carbon (TOC) contents using a Leco CS744 at the Faculty of Geoscience, University of Bremen, Germany. The

recoveries of the reference materials are 97.19% for PART NO. 502–914 Synthetic Carbon LCRM ($n = 1$) and 99.87 ± 0.44% for PART NO. 502-905 Synthetic Carbon LCRM (2SD, $n = 4$).

In order to date the cores and determine sedimentation and mass accumulation rates, ^{210}Pb was measured at 2 cm resolution. Freeze-dried sediment samples were sealed in petri dishes and left for 3 weeks to equilibrate the daughter isotopes of ^{226}Ra, ^{210}Pb, and ^{137}Cs and were afterward measured using a planar High Purity Germanium gamma detector (Canberra) at AWI. For details of the measurement, see Müller et al. (2025). The reference material IAEA-385 (Pham et al., 2008) was used to correct the activities for the detector efficiency. None of the cores reached zero excess ^{210}Pb ($^{210}Pb_{xs}$; incomplete inventory). We applied three different dating models: constant initial concentration (CIC) (Robbins, 1986), constant flux constant sedimentation (CFCS) (Krishnaswamy et al., 1971) and constant rate of supply (CRS) (Appleby & Oldfield, 1978), and corrected the latter for incomplete inventory (Appleby, 1998) as described in Supporting Information S1. We established a "quality matrix" and evaluated the best suitable model for each study site (Table S3 in Supporting Information S1) for further calculation of the sedimentation rates (Figure 5; Tables S4 and S6 in Supporting Information S1). To distinguish between local and lateral $^{210}Pb_{xs}$ and sediment input at the core sites, we calculated the focusing factor (Ψ; Figure 5; Table S5 in Supporting Information S1). The sediment accumulation rates (MAR_{Sed}) and the TOC accumulation rates (MAR_{TOC}) were calculated using the sedimentation rates derived from the CRS model as a recent study showed that the influence of change in MAR is best captured with the CRS model (Arias-Ortiz et al., 2018).

The quantification of SRR was performed by applying the whole-core injection method (Jørgensen, 1978; Røy et al., 2014) at the laboratory of GEOMAR Helmholtz Center for Ocean Research Kiel, Germany. Radiolabeled total reduced inorganic sulfur (TRIS) was separated from the sample using the cold chromium method (Kallmeyer et al., 2004; Røy et al., 2014), and the evolved H_2S was trapped as ZnS in 5 ml of 5% Zn acetate solution. Radioactivity in the sulfate and TRIS pools was analyzed using scintillation counting, and SRR was calculated according to Jørgensen (1978).

2.5. Statistical Analysis

Exploratory univariate analyses were conducted to assess potential relationships between Fe flux estimates and biogeochemical parameters (Table S7, Figure S7 in Supporting Information S1). Given the large uncertainties associated with flux estimates, these analyses are intended to highlight qualitative trends rather than to establish statistically robust controls. A Shapiro-Wilk test was performed prior to univariate statistical analysis (Shapiro & Wilk, 1965). Correlation coefficients were calculated using Pearson or Spearman correlation coefficients depending on the data distribution.

3. Results

3.1. Pore-Water Geochemistry

The sediment oxygen penetration depth (OPD) in KHB was generally lower than in CB: at KHB_{Fjord} it was 5 mm and at KHB_{Trough} 7.4 mm, while in CB the O_2 penetrated 8.5 mm into the sediment at the ice-proximal site (CBE_{Prox2}) and 15 mm at ice-distal sites (CB_{Confl}, CB_{Trough}) (Figures 2 and 3). In addition to the pore-water oxygen data, we report BW oxygen concentrations in Table S1 of Supporting Information S1 for context. In brief, the values ranged between 260.1 and 262.4 μM at KHB, slightly higher than in CB, where the values ranged from 231.2 to 259.8 μM. The highest dFe concentration of 658 μM was found at 16.5 cm at the ice-proximal site CBE_{Prox1a} (Figure 3a) compared to the ice-distal sites CB_{Confl} and CB_{Trough} where dFe concentrations of only up to 19 μM were determined (Figures 3c and 3d). The dFe profiles at the ice-distal sites at KHB and CB were more condensed compared to all other sites (Figures 2b and 3d). Furthermore, dFe concentrations only increased below 3.5 cm at the CBE sites (Figures 3a and 3b), whereas in KHB, at both sites, the profiles already revealed a sharp downward increase in the top 2 cm (Figures 2a and 2b). The dMn concentrations at both ice-distal sites (KHB_{Trough} and CB_{Trough}) (Figures 2b and 3d) were relatively low compared to dFe. At all other sites, including KHB_{Trough}, dMn peaks occurred above the dFe maxima, with a maximum concentration of 70 μM found at 4.5 cm at CBE_{Prox1a} (Figure 3a). In general, the concentrations of dMn were significantly lower at KHB compared to CB by one order of magnitude. Pore-water PO_4^{3-} concentrations increased with depth at all sites (Figures 2 and 3), but were higher in KHB (maximum concentration of 325 μM at 30 cm at KHB_{Fjord}) (Figure 2a) compared with CB (maximum concentration of 197 μM at 12 cm at CB_{Confl}) (Figure 3c). There was a noticeable change of slope in

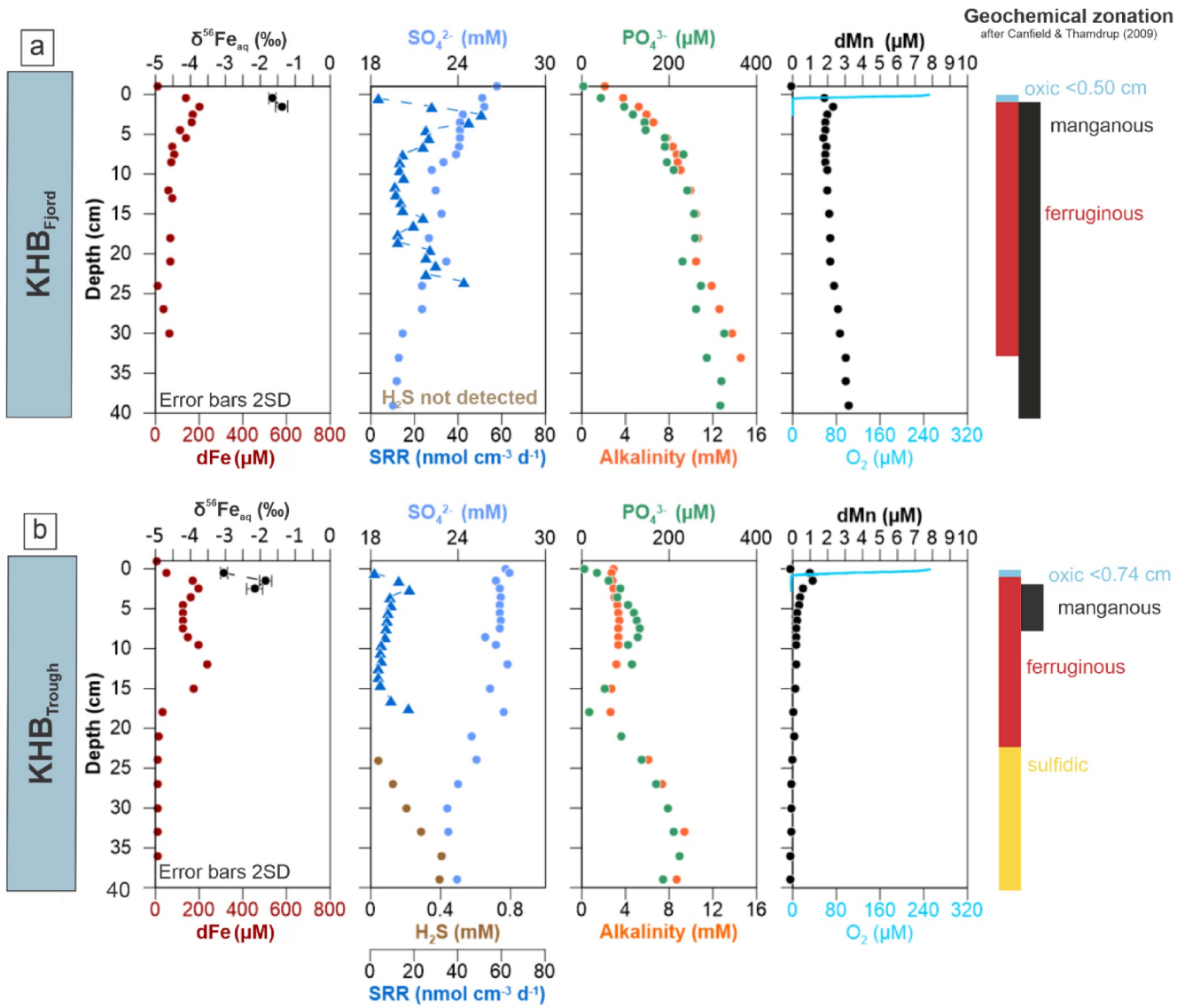

Figure 2. Pore-water and solid phase geochemical data for sites in King Haakon Bay (KHB): Dissolved Fe (dFe) concentrations (red), the isotopic signature of dFe ($\delta^{56}Fe_{aq}$, black) with the two-fold standard deviation (2SD) of replicate analyses, sulfate (SO_4^{2-}, blue), sulfate reduction rates (SRR, triangle, and smalt blue), phosphate (PO_4^{3-}, green), alkalinity (orange), hydrogen sulfide (H_2S, brown), dissolved Mn (dMn, black) and the oxygen concentration (O_2, turquoise). Left: name of coring site; right: geochemical zonation after Canfield and Thamdrup (2009).

the PO_4^{3-} profile at KHB_{Trough} with the concentrations dropping sharply to nearly zero between 15 and 20 cm (Figure 2b), coinciding with the lower boundary of the ferruginous zone. The lowest PO_4^{3-} concentrations occurred at the ice-proximal sites at CBE (Figures 3a and 3b). Alkalinity (Figures 2 and 3) and DIC (Figure S8 in Supporting Information S1) concentrations showed identical patterns and increased with depth. Only at site, KHB_{Trough}, the alkalinity concentrations were constant between 0 and 17 cm (Figure 2b). The SO_4^{2-} profiles in KHB decreased with increasing depth with a slight concave-down shape at KHB_{Trough} (27.3 mM at the top to 23.9 mM at the base) (Figure 2b), whereas at the CBE sites the downward decrease in SO_4^{2-} concentrations was least pronounced (27.6 mM at top to 27.3 mM at the base) (Figures 3a and 3b). Free hydrogen sulfide was only detected at sites CB_{Trough} (6.5–23 cm) (Figure 3d) and KHB_{Trough} (24–39 cm) (Figure 2b). At all sites, $\delta^{56}Fe_{aq}$ values were less than 0‰. The KHB_{Fjord} site showed pore-water $\delta^{56}Fe_{aq}$ values of -1.64 ± 0.06‰ at 0.5 cm and KHB_{Trough} revealed pore-water $\delta^{56}Fe_{aq}$ values -3.04 ± 0.10‰ at 0.5 cm, that is followed by a downcore increase to -2.16 ± 0.23‰ at 2.5 cm (Figure 2). At CB, the pore-water $\delta^{56}Fe_{aq}$ values at CBE_{Prox1a} were -3.09 ± 0.14‰ at 1.5 cm and at CB_{Trough} -0.98 ± 0.11‰ at 1.5 cm (Figure 3). At all sites except for CB_{Trough}, pore-water $\delta^{56}Fe_{aq}$

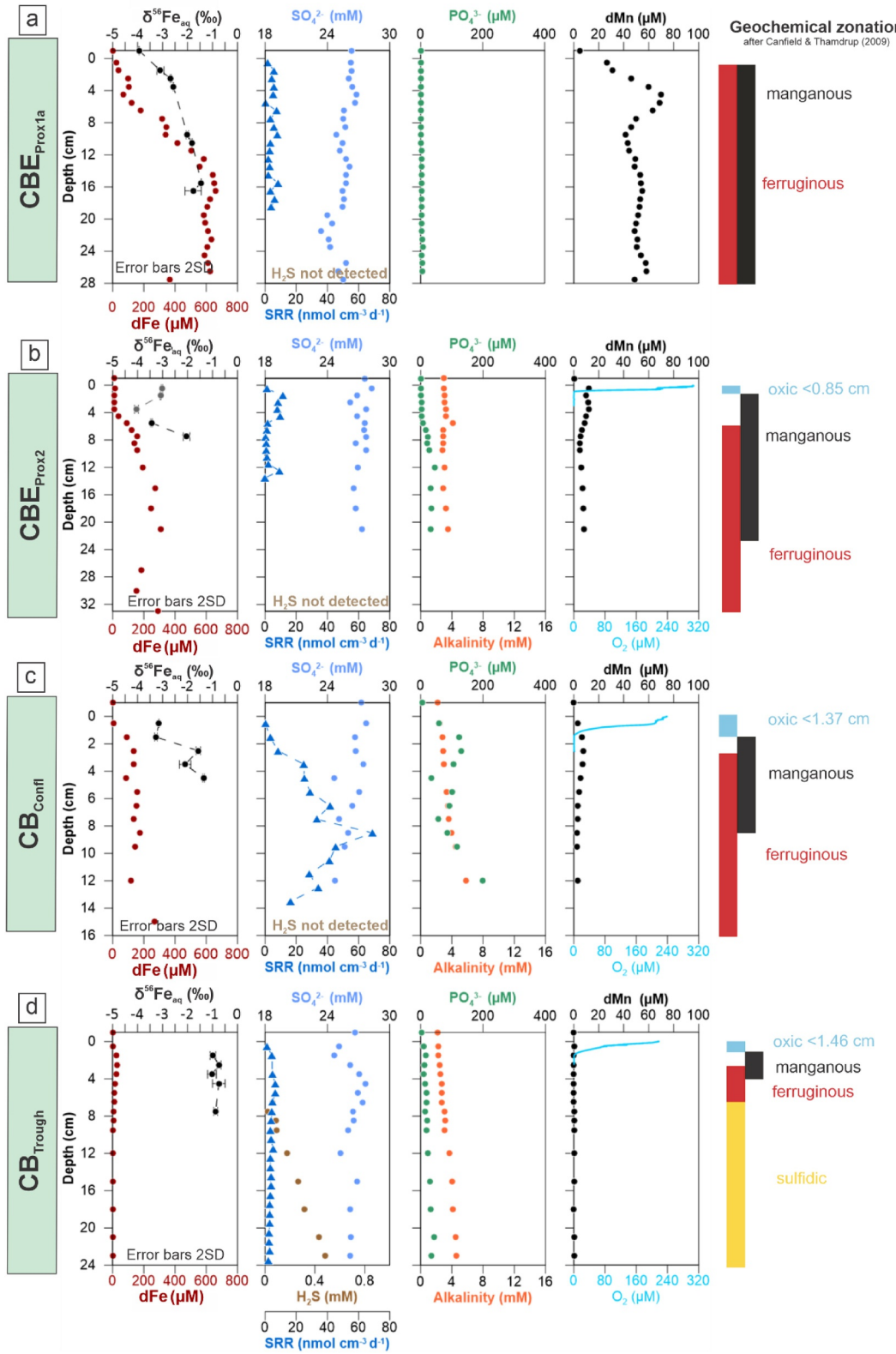

Figure 3. Pore-water and solid phase geochemical data for sites in Cumberland Bay (CB): Parameters and colors as indicated in Figure 2. Please note that the depth scales are adapted to the recovered interval and the dMn scale here is different than in Figure 2. (b) The data points shown in gray in the $\delta^{56}Fe_{aq}$ depth profile are those that exhibited poor recovery during the processing for Fe isotope analyses.

10.1029/2025GB008856

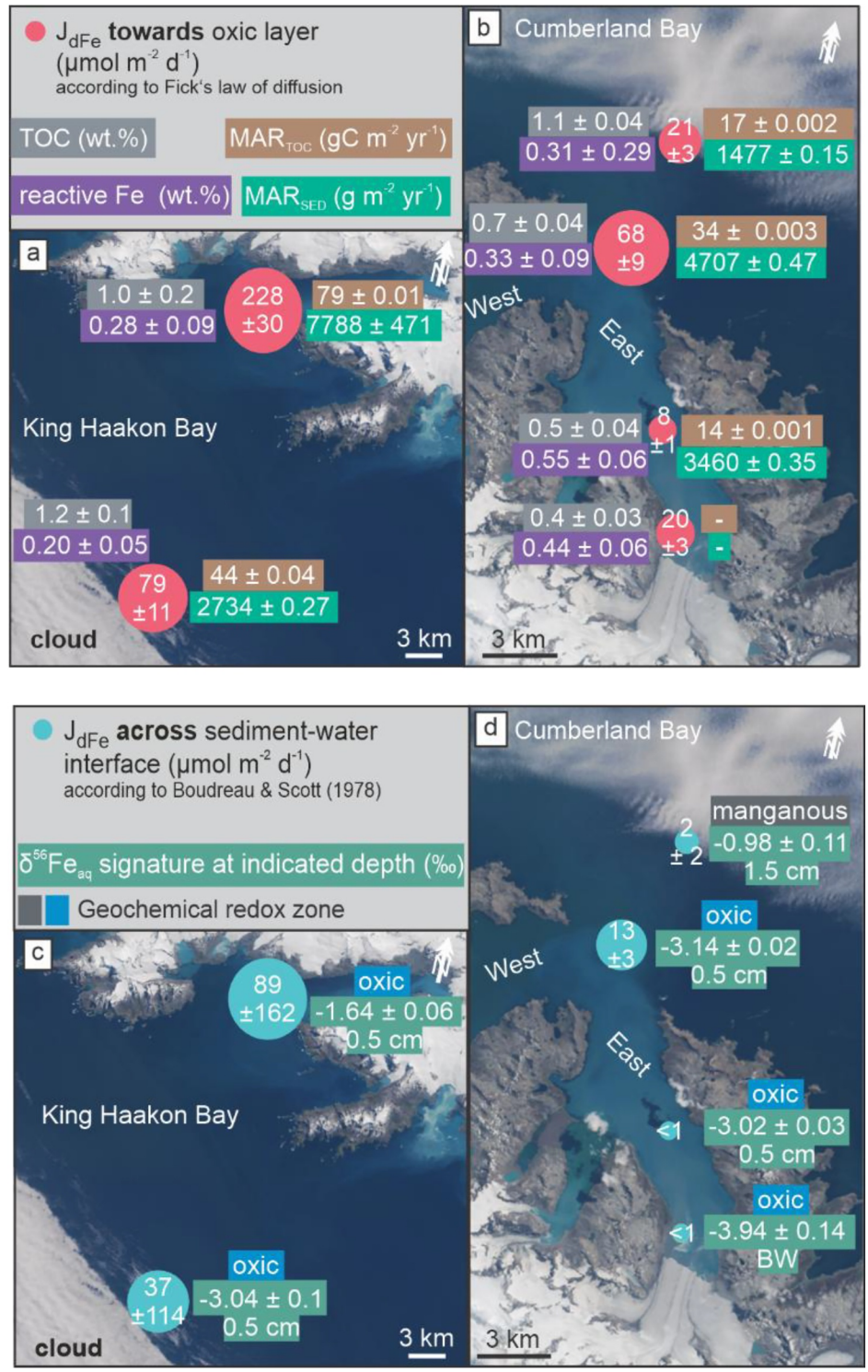

Figure 4. Satellite images of Cumberland Bay and King Haakon Bay. (a and b): Reddish circles show the J_{dFe} toward the oxic layer (µmol m^{-2} d^{-1}), calculated according to Fick's law of diffusion; gray: total organic carbon (TOC) content (wt.%) in the surface sediment (top few cm) (error given as twofold standard deviation [2SD]); purple: reactive Fe content (wt.%) in the surface sediment (top few cm) (error given as 2SD); green: sediment accumulation rate (g m^{-2} yr^{-1}) (error refers to mathematical propagation error); blue: TOC accumulation rate (gC m^{-2} yr^{-1}) (error refers to mathematical propagation error). (c and d) light green: $\delta^{56}Fe_{aq}$ at indicated depth (‰) (error given as 2SD) and respective geochemical redox zone. The blue circles show the benthic J_{dFe} across the sediment-water interface according to Boudreau and Scott (1978). Satellite image: Sentinel-2 L1C from 01/2023 (CBE) and from 11/2021 (KHB).

10.1029/2025GB008856

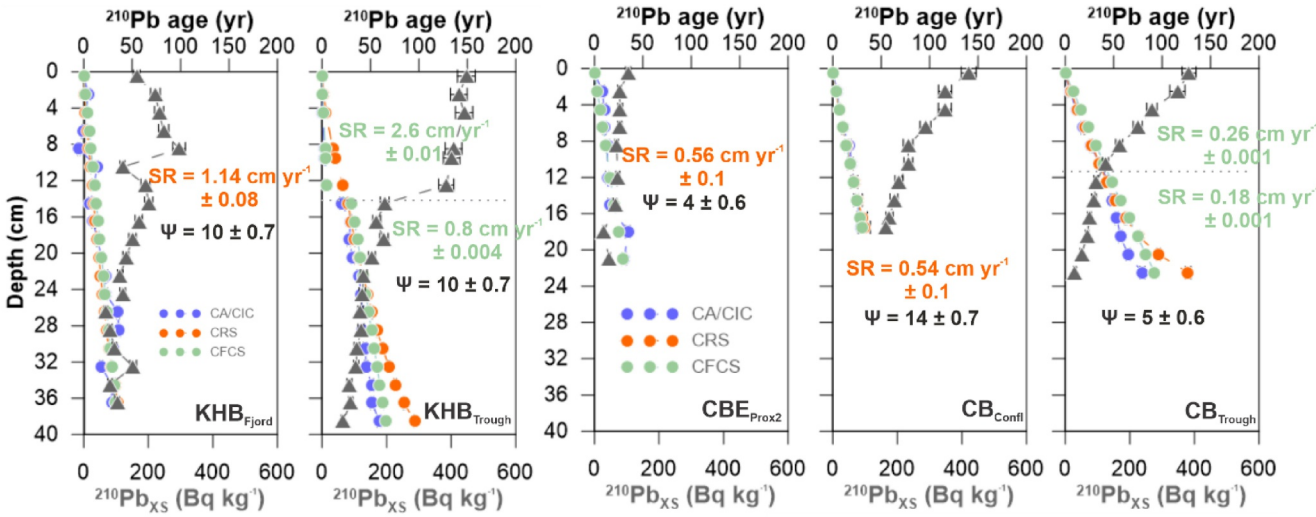

Figure 5. $^{210}Pb_{xs}$ activities for all core sites in dark gray (triangle). $^{210}Pb_{XS}$ age model calculated for all three models (circles): constant activity (CA)/constant initial concentration (CIC) (blue), constant rate of supply (CRS) (orange) and constant flux and constant sedimentation (constant flux constant sedimentation) (green). Left: King Haakon Bay (KHB). Right: Cumberland Bay (CB). Given sedimentation rates were calculated using the best suitable model according to the quality matrix (Tables S3 and S4 in Supporting Information S1). Ψ = Focusing factor (SI Sediment focusing, Table S5 in Supporting Information S1). The actual true error may differ. The error bar here refers to the mathematical propagation error.

increased with depth. At CB_{Trough}, the pore-water $\delta^{56}Fe_{aq}$ values were rather constant (mean value of $-0.87 \pm 0.07‰$, $n = 4$) with depth. Only at CBE_{Prox1a}, a BW $\delta^{56}Fe_{aq}$ value was measured. There, BW $\delta^{56}Fe$ exhibited a signature of $-3.94 \pm 0.14‰$, which is lower than the uppermost pore-water $\delta^{56}Fe_{aq}$ value with $-3.09 \pm 0.14‰$ at 1.5 cm. At the other sites, the dFe concentrations of the BW were too low to produce reliable data. In Figure 4, the uppermost obtained $\delta^{56}Fe_{aq}$ value is given depending on the available volume and processing feasibility.

3.2. Diffusive Iron Fluxes and pH

The pH of the BW (Table S2 in Supporting Information S1) varied from the lowest values of 6.9 ± 0.4 at KHB_{Fjord} to 7.6 ± 0.6 at CBE_{Prox2} (Figure S8 in Supporting Information S1). In CB, the $J_{dFe\ towards\ oxic\ layer}$ were ranged at the ice-proximal sites from 8 ± 1 (CBE_{Prox2}) to 20 ± 3 μmol m^{-2} d^{-1} (CBE_{Prox1a}) and 21 ± 3 μmol m^{-2} d^{-1} at CB_{Trough}, and were slightly higher at the distal site CB_{Confl} (68 ± 9 μmol m^{-2} d^{-1}) (Figure 4b). At KHB, the $J_{dFe\ towards\ oxic\ layer}$ were 228 ± 30 (KHB_{Fjord}) and 79 ± 11 μmol m^{-2} d^{-1} (KHB_{Trough}) (Figure 4a). At CB, the $J_{dFe\ across\ SWI}$ were considerably lower. For the ice-proximal sites, we determined $J_{dFe\ across\ SWI} < 1$ μmol m^{-2} d^{-1} for CBE_{Prox1a} and CBE_{Prox2}. For the ice-distal sites, the $J_{dFe\ across\ SWI}$ were 13 ± 3 at CB_{Confl} and 2 ± 2 μmol m^{-2} d^{-1} at CB_{Trough} (Figure 4d). The $J_{dFe\ across\ SWI}$ were 37 ± 114 at KHB_{Trough} and 89 ± 162 μmol m^{-2} d^{-1} at KHB_{Fjord} (Figure 4c).

3.3. Iron Extractions

The depth-distribution of the 0.5 M HCl extractable $Fe(II)_s$ and $Fe(III)_s$ can be found in Figure S10 of Supporting Information S1. To compare the sites between each other, we averaged the results of reactive $Fe(II)_s$ and $Fe(III)_s$ to the depth where we found the maximum of the dFe as indicated in Figure S10 of Supporting Information S1. At both ice-proximal sites at CBE, the 0.5 M HCl extractable ('reactive') $Fe(III)_s$ ranged from 0.44 ± 0.06 wt.% to 0.55 ± 0.06 wt.% (CBE_{Prox1a} and CBE_{Prox2}, respectively). Contents were slightly lower at the ice-distal sites with 0.33 ± 0.09 wt.% at CB_{Confl} and 0.31 ± 0.29 wt.% at CB_{Trough} (Figure 4b). At KHB, the "reactive" $Fe(III)_s$ content was lower with 0.28 ± 0.09 wt.% at KHB_{Fjord} and 0.20 ± 0.05 wt.% at KHB_{Trough} (Figure 4a). At the ice-proximal sites, the 0.5 M HCl-extractable $Fe(II)_s$ was 0.23 ± 0.04 wt.% (CBE_{Prox1a}) to 0.24 ± 0.05 wt.% (CBE_{Prox2}) with similar contents at CB_{Confl} (0.25 ± 0.08 wt.%). The lowest surface contents of 0.5 M HCl-extractable $Fe(II)_s$ were found at the CB_{Trough}.

3.4. Porosity and Total Organic Carbon

Porosities at the sediment surface ranged from 0.46 to 0.90, with lowest values at the ice-proximal sites at CBE and highest values at the ice-distal site CB_{Confl} and both sites in KHB (Table S1, Figure S9 in Supporting Information S1). The TOC contents were measured from core top to the dFe maximum and are given in the following as averaged values to the depth of the dFe maximum. TOC remained almost constant with depth at all sites (Figure S9 in Supporting Information S1), with lowest contents of 0.41 ± 0.03 wt.% at CBE_{Prox1a} and 0.44 ± 0.04 wt.% at CBE_{Prox2} (Figure 4b). There was an increase in TOC contents with distance from the glacier terminus, reaching 0.73 ± 0.04 wt.% and 1.12 ± 0.04 wt.% at CB_{Confl} and CB_{Trough}, respectively. At KHB, the TOC contents are generally higher compared to CBE (1.02 ± 0.18 wt.% at KHB_{Fjord} and 1.2 ± 0.06 wt.% at KHB_{Trough}; Figure 4a).

3.5. Age Model, Sedimentation Rates, and Mass and TOC Accumulation Rates

In CB, the lowest $^{210}Pb_{xs}$ activities at the top of the sediment cores were determined at the ice-proximal sites at CBE_{Prox2} with 104.8 ± 8.3 Bq kg^{-1} with an increasing trend toward the ice-distal sites with 420.9 ± 23.3 Bq kg^{-1} (CB_{Confl}) and 383.6 ± 21.7 Bq kg^{-1} (CB_{Trough}) (Figure 5). The same trend was observed at KHB with 164.2 ± 10.4 Bq kg^{-1} (KHB_{Fjord}) and 447.2 ± 27.6 Bq kg^{-1} (KHB_{Trough}) (Figure 5). At CB, all profiles showed an exponential $^{210}Pb_{xs}$ decline with depth with the exception of CBE_{Prox2} (Figure 5). In KHB, the $^{210}Pb_{xs}$ profiles are stair-stepped (Figure 5). At KHB_{Fjord}, the $^{210}Pb_{xs}$ activity declined less pronouncedly, still displaying 103.9 ± 6.8 Bq kg^{-1} at the core bottom. The age models for all cores bear uncertainties regarding the dating model assumptions. ^{137}Cs as an independent time marker was not detectable at any core site, probably related to the generally lower concentrations in sub-Antarctic sediments (Godoy et al., 2024). The overall good agreement (Figure 5) of all three age models (CA/CIC, CRS, and CFCS) for all cores demonstrates that the results are reliable. In general, the sedimentation rates decreased from ice-proximal to ice-distal sites at CB with overall higher rates of 2.6 cm yr^{-1} (KHB_{Trough}) and 1.14 cm yr^{-1} (KHB_{Fjord}) at the sites in KHB compared to CB from 0.26 to 0.56 cm yr^{-1} (Figure 5). The MAR_{Sed} was highest at CB_{Confl} and KHB_{Fjord} and lowest at the trough sites CB_{Trough} and KHB_{Trough} (Figures 4a and 4b; Table S4 in Supporting Information S1). The MAR_{TOC} revealed highest values of 34 (CB_{Confl}), 44 (KHB_{Trough}) and 79 gC m^{-2} yr^{-1} (KHB_{Fjord}) and lowest at the ice-proximal site at CBE_{Prox2} with 14 gC m^{-2} yr^{-1} (Figures 4a and 4b).

3.6. Sulfate Reduction Rates

The SRRs at KHB were highest at KHB_{Fjord} with a sharp downward increase at the surface with a maximum of 51 nmol SO_4^{2-} cm^{-3} d^{-1} at 2.5 cm and a constant value with depth (Figure 2a). At the base (23.5 cm) at KHB_{Fjord}, an increase of 43 nmol SO_4^{2-} cm^{-3} d^{-1} was measured. At KHB_{Trough} the obtained SRRs were lower with a slight increase from surface to 4.5 cm depth, where 10 nmol SO_4^{2-} cm^{-3} d^{-1} are reached. The SRRs were lower at the ice-proximal sites at CB with 1 nmol SO_4^{2-} cm^{-3} d^{-1} at the surface and with no significant depth variation at CBE_{Prox1b} (Figure 3a). Similar to KHB_{Trough}, at CBE_{Prox2} the SRRs increased from surface to 4.5 cm depth with a peak of 10 nmol SO_4^{2-} cm^{-3} d^{-1} (Figure 3b) and the lowest SRRs were measured at CB_{Trough} with no significant depth-related increase and a maximum of 7 nmol SO_4^{2-} cm^{-3} d^{-1} at 5.5 cm (Figure 3d). The CB_{Confl} increased with depth to a maximum of 69 nmol SO_4^{2-} cm^{-3} d^{-1} at 8.5 cm (Figure 3c).

4. Discussion

In our study area, we observed spatial inter- and intra-fjord variability of benthic Fe fluxes (Figure 4) and associated pore-water $\delta^{56}Fe_{aq}$ values. In the following section, we discuss (a) the effects of the depositional conditions such as accumulation rates and early diagenetic processes in the fjord sediments of CB and KHB in order to decipher the primary drivers of Fe fluxes and (b) the reliability of the pore-water $\delta^{56}Fe_{aq}$ as a proxy for benthic Fe fluxes.

4.1. Depositional Regime

The sedimentation rates in CB are overall lower than in KHB (Figure 5) and also lower compared to similar settings such as King George Island in the Antarctic (Monien et al., 2014) and Kongsfjorden in the Arctic (Herbert et al., 2021). Sites at the glacier terminus are often characterized by high sedimentation rates (Syvitski, 1989). Based on observational data, the Nordenskjöld Glacier in the CB recently revealed lower retreat rates in the last

few years compared to the previous decades (Farías-Barahona et al., 2020); however, the unusually low sedimentation rates at CBE_{Prox2} indicate that the area close to the glacier is not the primary deposition area of sediment. At CBE, satellite imagery from the East Bay reveals brown-colored turbid sediment plumes (Figure S12a in Supporting Information S1), providing further evidence of the primary deposition area being farther away from the glacier terminus. The sediment discharges probably originate from subglacial meltwater plumes from the marine-terminating Nordenskjöld Glacier. At KHB, the brownish sediment plume is observed on the northern shore, where it seems to emanate from proglacial meltwater streams (Figure S12b in Supporting Information S1). The sedimentation rates at CB_{Confl} are similarly low compared to CBE_{Prox2}, but $^{210}Pb_{xs}$ activities are significantly higher with an exponential decline, suggesting steady-state accumulation. Intriguingly, sediment focusing at this site is the strongest of all investigated sites (Figure 5). As CB_{Confl} is located at the confluence zone merging the West- and East Bays of CB, this site might act as a sediment deposition center, where the lateral contribution of glacial material from both bays dominates the sedimentation rates. The lowest observed sedimentation rates in our study area were found at the CB_{Trough} (0.26 cm yr^{-1}) and are most likely a result of low-energy deposition in the trough and are characterized by minimal sediment mixing (evident in $^{210}Pb_{xs}$ profiles and low mixing coefficients shown in the SI). Further, CB_{Trough} receives glacially derived sediments via sporadic events rather than continuously, which has been observed in similar settings in subpolar fjords (Boldt et al., 2013). At KHB the sedimentation rates are generally higher and the rather constant $^{210}Pb_{xs}$ profile from 0 to 14 cm at KHB_{Trough} indicates rapid deposition. This is supported by the distinct change in slope observed in the pore-water profiles (Figure 2b) at a depth of 14 cm; a constant alkalinity (0–14 cm) and strong sediment focusing (Figure 5) indicate significant sediment re-distribution. Both KHB sites reveal strong sediment focusing, which hints toward a more dynamic sedimentary regime at KHB compared to CB (except at CB_{Confl}).

An overall substantial spatial variability of the MAR_{TOC} across both fjords can be observed (Figure 4). This finding is in agreement with a recent study by Berg et al. (2021) on CB sediments, where variable MARs were reported. Low MAR_{TOC} in proximity to the glacier (Figure 4b) at CBE_{Prox2} might be a consequence of low primary production, due to high turbidity in the water column, leading to low carbon export to the sediment. In combination with high sedimentation rates of inorganic material, this creates low TOC, limiting the respiration of benthic organisms. The higher MAR_{TOC} at CB_{Confl} aligns with the findings of a recent study stating that marine organic carbon (autochthonous biospheric pool) increases with increasing distance from the Nordenskjöld Glacier (Berg et al., 2021). Our data of higher TOC contents at the ice-distal sites (CB_{Confl}, CB_{Trough}, KHB_{Fjord}, and KHB_{Trough}), in combination with the findings by Berg et al. (2021), are a consequence of the increased carbon supply from primary productivity compared to the ice-proximal sites, which was also observed in similar settings on Svalbard (Laufer-Meiser et al., 2021). Compared to the CB sites, both KHB sites have higher PO_4^{-3} concentrations and SRR, which are known to be controlled by organic carbon burial rates (Jørgensen, 1978; Zhou et al., 2023). The overall higher TOC in KHB sediments together with higher chlorophyll-*a* concentrations observed in KHB during the campaign point to a higher primary productivity in the water column, resulting in higher carbon export to the sediments. Although the reactivity of organic carbon is generally controlled its origin (e.g., Freitas et al., 2021; Wei et al., 2025; Xu et al., 2023; Zonneveld et al., 2010), we mainly ascribe the spatial variability of MAR_{TOC} to sediment focusing as this process was hypothesized to increase MAR_{TOC} (Burdige, 2007; Canfield, 1994; Müller et al., 2025; Steinsberger et al., 2017) and as at three sites - CB_{Confl}, KHB_{Trough} and KHB_{Fjord}—are notable for their strong sediment focusing and their high MAR_{TOC}. In addition, the variation of the oxic layer thickness is primarily controlled by the MAR_{TOC}, which governs the geochemical redox zonation (e.g., Froelich et al., 1979; Jørgensen et al., 2005; Müller et al., 2025, 2026). The higher the MAR_{TOC}, the faster O_2 is depleted during organic matter degradation and hence the OPD decreases. This can be observed at both KHB sites, where MAR_{TOC} (14–34 gC m^{-2} yr^{-1}) exceeds and leads to OPDs <1 cm. In CB, lower MAR_{TOC} (44–79 gC m^{-2} yr^{-1}) resulted in OPDs >1 cm. In summary, both fjords exhibit dynamic depositional environments, with the sites CB_{Confl}, KHB_{Trough}, and KHB_{Fjord} particularly notable for their high MARs and strong sediment focusing.

4.1.1. Reactive Iron Supply

Generally, higher reactive Fe contents were found at CB compared to KHB (Figures 4a and 4b). As indicated by other studies performed in the Arctic, the catchment geology (Wehrmann et al., 2014) and thus, the weathering processes at the ice-rock interface determine the supply of Fe phases into the fjords (Tranter & Wadham, 2014; Wadham et al., 2010). The catchment at CB contains Fe-rich sandstone (Curtis, 2011) and therefore could be an

important source of Fe oxides to the fjord. The andesitic volcanoclastic rocks of KHB are richer in silica and likely supply sediments with lower Fe contents leading to overall lower reactive Fe contents at KHB compared to CB. In addition, fjords usually show dynamic sedimentation patterns, influenced by bathymetry and distinct water dynamics (turbidity, BW currents), which create spatial differences in the supply, distribution and deposition of reactive Fe (Bianchi et al., 2020; Monien et al., 2017; Syvitski, 1989). At CB_{Confl}, CB_{Trough} and both KHB sites, Fe-phases might have been delivered by nepheloid layers (Biscaye & Eittreim, 1977), which can transport fine-grained material farther from the glacier terminus. The reason for the overall lower reactive Fe contents at the investigated KHB sites could thus be the larger distance to the Brigg's Glacier terminus and the respective sediment plume compared to the CBE. Additionally, at KHB, the plumes originate from proglacial meltwater streams. During transport through the proglacial environment, approximately 80% of dFe flocculates and/or precipitates (Zhang et al., 2015), reducing the amount delivered to the fjord. Consequently, fewer solid Fe phases reach the fjord at KHB due to prior deposition within the meltwater stream and/or aging of the solid phase (Zhao et al., 2022). External input of reactive Fe and benthic cycling are the main drivers for controlling the amount of reactive Fe in subsurface sediments of glaciated fjords (Laufer-Meiser et al., 2021). Supply of reactive Fe promotes microbial Fe reduction (Laufer-Meiser et al., 2021; Raiswell et al., 2006), during which organic matter is oxidized while Fe-oxides are reduced (Froelich et al., 1979). At the glacier terminus at CBE, both sites reveal high reactive Fe and comparably low TOC contents. Despite the high supply of reactive Fe, microbial iron reduction is slow, likely due to the low TOC content (Figures 4a and 4b). With increasing distance from the glacier terminus at CB_{Confl} and CB_{Trough}, the reactive Fe content decreases, while the TOC increases at still lower sedimentation rates, creating more favorable conditions for microbial Fe reduction. Notably, a correlation was observed between the reactive Fe content and the TOC content ($R^2 = 0.76$, p-value <0.05) as both are needed to facilitate microbial Fe reduction. At both trough sites (CB_{Trough}, KHB_{Trough}), higher MAR_{TOC} resulted in a more condensed redox zonation. Hence, a key factor determining the dFe accumulation at depth is the sedimentation, which, at low rates, leads to a deeper dFe accumulation or, at high rates, to a condensed redox zonation.

Overall, our data suggest different extents of reactive Fe supply into the investigated fjord sediments. While the catchment geology and transport pathway (subglacial discharge vs. meltwater stream) determine the supply of reactive Fe phases into fjords, as also elaborated by Henkel et al. (2018), distinct depositional regimes govern the spatial distribution of the reactive Fe phases, where the MAR_{TOC} controls the redox zonation and hence the depth and extent of the dFe accumulation.

4.2. Early Diagenetic Redox Processes and the Iron Isotope Signature of Pore-Water

We found a broad range of pore-water and BW $\delta^{56}Fe_{aq}$ values of the uppermost measured surface sediment and the BW in both fjords, ranging from $-3.94 \pm 0.14‰$ in the BW (oxic) at CBE_{Prox1a} to $-0.98 \pm 0.11‰$ at 1.5 cm (manganous zone) at the CB_{Trough} (Figures 4c and 4d). It is crucial to compare pore-water data from equivalent redox zones as dFe diffuses upward along its concentration gradient, and when it crosses a redox boundary (e.g., from a manganous to an oxic zone), the chemical reactions it undergoes change. These redox transitions are associated with isotopic fractionation (Johnson & Beard, 2005). Consequently, pore-water of different redox zones (e.g., oxic vs. manganous) will inherently display different pore-water $\delta^{56}Fe_{aq}$ signatures. In the following chapter, we discuss this in terms of a variety of isotope fractionation processes (where possible) and the respective mass balances, where the isotopic variability between these two pools (ferric substrate vs. ferrous pore-water) is determined by their respective size of them and the bulk sedimentary Fe pool.

We identified four processes that are known to lead to Fe isotope fractionation resulting in a broader range close to the SWI pore-water $\delta^{56}Fe_{aq}$ values (Johnson & Beard, 2005), including (a) microbial Fe reduction (Crosby et al., 2007), (b) reaction of dFe with hydrogen sulfide and precipitation of Fe sulfides (Butler et al., 2005), (c) re-oxidation of sulfide to sulfate (McAnena et al., 2024) and (d) re-oxidation and precipitation of dFe above the iron reduction zone (Beard & Johnson, 2004; Staubwasser et al., 2013). In particular, iron isotopic fractionation factors related to either microbial Fe reduction ($\Delta^{56}Fe_{Fe(III)reac–Fe(II)aq} = 2.95 \pm 0.68‰$) (Crosby et al., 2007) or the reaction of ferrous Fe phases with dissolved sulfide ($\Delta^{56}Fe_{Fe(II)aq–FeS} = 0.85 \pm 0.30‰$) (Butler et al., 2005) are distinct, allowing to differentiate these processes in nature (Severmann et al., 2010). A recent study on the abiotic reductive dissolution of Fe (oxyhydr)oxide by HS^- demonstrated that this process preferentially releases light Fe isotopes into the pore-water in marine anoxic settings (McAnena et al., 2024).

The lowest pore-water $\delta^{56}Fe_{aq}$ values in the oxygenated BW in our study area were found at CBE_{Prox1a} (Figure 4d), accompanied by low dFe concentrations. A trend toward heavier isotopes with increasing depth as it has been described for other settings (Henkel et al., 2018; Severmann et al., 2010; Staubwasser et al., 2006) was observed at sites CBE_{Prox1a}, CBE_{Prox2}, and CB_{Confl}. The strongest depletion of $\delta^{56}Fe_{aq}$ is usually found at the sediment surface where microbial Fe reduction (e.g., Henkel et al., 2018; Staubwasser et al., 2006) and oxidation of dFe (e.g., Bullen et al., 2001; Welch et al., 2003) are most intense. As microbial Fe reduction progresses with depth, $Fe(III)_s$ becomes increasingly enriched in ^{56}Fe. Consequently, pore-water $\delta^{56}Fe_{aq}$ increases with depth too, as $^{54}Fe(III)_s$ becomes less accessible (Crosby et al., 2007; Staubwasser et al., 2006). This can be observed at both CBE sites, CB_{Confl} (Figures 3a–3c) and at the KHB_{Trough} (Figure 2b).

At CB_{Trough} the isotopic signature reveals heavier pore-water values at the surface with $-0.98 \pm 0.11‰$ at 1.5 cm (manganous zone) (Figure 4d) and is characterized by a condensed redox zonation with a broad sulfidic zone (Figure 3d). The overall heavier signature of the pore-water $\delta^{56}Fe_{aq}$ points to Fe-S interaction. Hydrogen sulfide, which reacts to Fe monosulfides (FeS) and potentially pyrite (FeS_2), acts as a sink of dFe in the pore-water (e.g., Jørgensen, 2021; Jørgensen & Kasten, 2006; Rickard, 1997; Riedinger et al., 2014). Iron monosulfides formed during the reaction of dFe with H_2S preferentially incorporate light isotopes (Butler et al., 2005). Similar to CB_{Trough}, the pore-water $\delta^{56}Fe_{aq}$ at KHB_{Fjord} is slightly heavier with $-1.06 \pm 0.04‰$ at 1.5 cm (ferruginous-manganous zone). We propose that slightly heavier signals at KHB_{Fjord} were produced due to the formation of FeS. The presence of FeS was indicated by a dark color of the sediment beneath 2 cm depth (Figure S11b in Supporting Information S1) and by higher AVS contents (Figure S10 in Supporting Information S1). This is consistent with an increase of SRRs beneath the sediment surface (Figure 2a) and the absence of free sulfide that would otherwise lead to FeS_2 formation, as seen at station CB_{Trough}.

At KHB_{Trough}, the pore-water $\delta^{56}Fe_{aq}$ value of $-1.85 \pm 0.18‰$ at 1.5 cm (ferruginous-manganous zone) is light compared to the same zone at CB_{Trough} ($-0.74 \pm 0.08‰$ at 2.5 cm) (ferruginous-manganous zone). We hypothesize that more recycled reactive $Fe(III)_s$ are deposited at the SWI at KHB_{Trough}, that may be heavier than dFe, changing the initial isotopic baseline from which redox processes begin. This aligns with the light pore-water $\delta^{56}Fe_{aq}$ value of $-3.04 \pm 0.10‰$ at 0.5 cm (oxic zone) at KHB_{Trough}. We note that the reactive Fe content at the surface at CB_{Trough} with 0.31 wt.% and at KHB_{Trough} with 0.20 wt.% does not support the theory of more recycled reactive Fe at KHB_{Trough}, but the more dynamic depositional environment at KHB_{Trough} does. At KHB_{Trough}, more dynamic depositional conditions likely promote its role as a depocenter for diagenetically recycled material transported from fjords, reflected by higher sedimentation rates and an elevated focusing factor (Figure 5). Additionally, lower sedimentation rates and hence a longer retention time of Fe oxides in the sediment result in a heavier signature of aqueous and solid Fe. A heavier pore-water $\delta^{56}Fe_{aq}$ value is visible at CB_{Trough}, where the less dynamic depositional environment exists (elaborated in detail in 4.1.) favors the Fe-S interactions dominating the pore-water $\delta^{56}Fe_{aq}$ signature.

We note that sedimentary diagenesis contributes to the observed pore-water $\delta^{56}Fe_{aq}$ signals, but differences in the isotopic composition of the solid Fe phase delivered to the sediments, hence sediment provenance, may also control the initial pore-water signature. Therefore, the pore-water $\delta^{56}Fe_{aq}$ signature reflects a combination of the effects of sediment provenance, benthic recycling and fractionation during biotic and abiotic processes.

4.3. Primary Driver of Benthic Iron Fluxes

Three scenarios emerge from this study, given in a schematic overview of the early diagenetic processes and depositional conditions affecting the pore-water $\delta^{56}Fe_{aq}$ composition and the magnitude of the Fe fluxes differently (Figure 6). The three scenarios are: (a) oxic retention of Fe, (b) optimal Fe release, and (c) sulfidic retention of Fe. In our study area, three sites, CB_{Confl}, KHB_{Trough}, and KHB_{Fjord}, are identified as having a balanced depositional regime and biogeochemical conditions for maximal benthic Fe release (Figure 6). MAR_{TOC} revealed a positive association with $J_{dFe\ towards\ the\ oxic\ layer}$ and $J_{dFe\ across\ the\ SWI}$ (Figure S7 in Supporting Information S1). The benthic Fe fluxes depend on MAR_{TOC}, which determines the position of redox zones within the sediment. Steinsberger et al. (2017) investigated deep lake sediments from different locations and identified a relationship between the benthic Fe fluxes from the sediment and the local MAR_{TOC}, which aligns with our findings. It is estimated that over ~90% of the diffusive Fe flux becomes trapped in the sediments due to ongoing

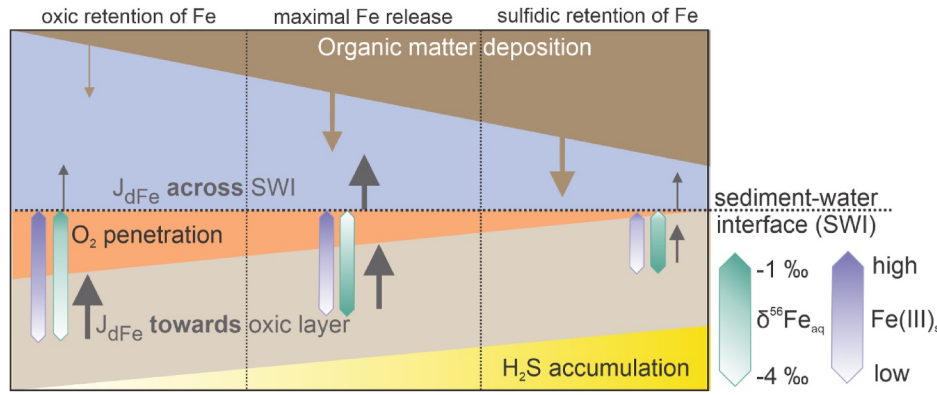

Figure 6. Conceptual model for our study area of the early diagenetic processes close to the sediment-water interface affecting the Fe isotopic signature (green bar). Three scenarios are given: (a) oxic retention of Fe, (b) maximal Fe release, and (c) sulfidic retention of Fe. The purple bar indicates the reactive Fe content in the surface sediments. Thickness of arrows indicates the magnitude of the respective fluxes. Green bar shows the iron isotopic signature below the oxic zone.

re-oxidation, preventing its release into the water column (Burdige & Komada, 2020; Elrod et al., 2004). For the investigated sites here, the range of the prevented release relative to the $J_{dFe\ towards\ SWI}$ of dFe due to oxidation close to the SWI is between ~53% and 88% (Figures S2a–S2f in Supporting Information S1) and is likely related to the shallower OPD at KHB as a result of the depositional regime (details given in Section 4.1). The three sites with maximal benthic Fe release reveal more condensed redox zones and consequently a shallower OPD. At three sites, pH and SRR show a pronounced increase at the sediment surface. Within this interval, $J_{dFe\ towards\ oxic\ layer}$ estimates decrease with increasing pH, although this pattern is accompanied by uncertainty and is interpreted qualitatively (Figure S7, Table S7 in Supporting Information S1). Sulfate reduction has an effect on pH as the pH increases during sulfide formation (Ben-Yaakov, 1973; Soetaert et al., 2007). Sulfate reduction rates may influence dFe accumulation in surface sediments and contribute qualitatively to the variability in $J_{dFe\ across\ the\ SWI}$ estimates (Figure S7, Table S7 in Supporting Information S1). The SRRs increase with increasing organic carbon availability (Michaud et al., 2020), which can be observed in our study area, where peaks in SRRs close to the sediment surface align with dFe peaks (Figures 2 and 3) and comparably higher MAR_{TOC}. The produced H_2S during SRR can reduce Fe-oxides delivered by the glacier (Michaud et al., 2020), increasing the $J_{dFe\ across\ SWI}$, which was also observed by Herbert et al. (2021). Another key driver of high $J_{dFe\ across\ SWI}$ is sediment focusing leading to high deposition of ample organic material and reactive Fe and hence increasing the MAR_{TOC}. Scholz et al. (2014) elaborated that high $J_{dFe\ across\ SWI}$ are generated in a very narrow "redox window," where no oxygen and minor sulfide are present in surface sediments, as also observed in other studies (Lenstra et al., 2021). This aligns with our findings where we find the highest $J_{dFe\ across\ SWI}$ with a high enough content of reactive Fe and TOC to favor iron reduction but low enough sulfate reduction to fully precipitate all dFe as FeS. The reactive Fe content is inversely associated with $J_{dFe\ towards\ the\ oxic\ layer}$ but not with $J_{dFe\ across\ the\ SWI}$ (Figure S7, Table S7 in Supporting Information S1).

At CB_{Confl}, adjacent cores exhibit flux variations spanning two orders of magnitude. The first-order rate constant for Fe oxidation was calculated for a pH range of 6.5–8 for all sites (Figure S3 in Supporting Information S1). Within this model parameterization, Equation 4 describes a non-linear increase in k_1 with increasing pH. Above pH ~7.2, k_1 becomes increasingly sensitive to changes (Equation 5). At lower pH levels, a slowdown of the Fe oxidation rate promotes the escape through the oxic layer (Equation 4). Since the pH is calculated using DIC and alkalinity, it may differ from the true value, which is consistent with the error estimation we performed (Table S2 in Supporting Information S1). This generally known discrepancy has been evaluated in detail by Takeshita et al. (2020). The $J_{dFe\ across\ SWI}$ was calculated for a pH range of 6.5–8 (Figure S4 in Supporting Information S1), which is the observed pH range for pore-water in shelf sediments sustaining anoxic diagenesis (pH range 6.9–8.3 in Ben-Yaakov, 1973). Across this pH range, the modeled Fe flux estimates vary by five orders of magnitude. Variations among sites are most pronounced at pH < 7.5, showing the high sensitivity of benthic Fe flux estimates to pH values.

4.4. Consequences for the Use of Stable Iron Isotopes Identifying Benthic Iron Fluxes

Sites with lowest $J_{dFe\ across\ SWI}$ (both CBE sites and CB_{Trough}) show a broader range of the pore-water $\delta^{56}Fe_{aq}$ signatures close to the SWI. Low $J_{dFe\ across\ SWI}$ can be generated either due to (a) the low production of dFe or (b) a drawdown of dFe by sulfide formation or (c) Fe oxide precipitation within the oxic zone. Where $J_{dFe\ across\ SWI}$ are higher (KHB and CB_{Confl}), the pore-water $\delta^{56}Fe_{aq}$ signatures are less variable. From this, two important aspects emerge: (a) If the shallowest sediments reveal a narrow oxic zone and high concentrations of dFe, the BW $\delta^{56}Fe_{aq}$ signal likely reflects the isotopic signature of the dominant reductive process. (b) As the oxic zone extends and Fe precipitation close to the SWI plays an increasing role in the pore-water $\delta^{56}Fe_{aq}$ composition, the range in pore-water $\delta^{56}Fe_{aq}$ close to the SWI increases. Figure S7f in Supporting Information S1 shows the relationship between benthic Fe efflux and the $\delta^{56}Fe_{aq}$ signal of the oxic zone. Low-efflux sites generally display lighter $\delta^{56}Fe_{aq}$ values in the oxic zone (except CB_{Trough}). However, due to their low fluxes, these sites contribute little to the overall 'benthic efflux signature' in bottom waters. This interpretation is supported by the flux-weighted average $\delta^{56}Fe_{aq}$ signature of the $J_{dFe\ across\ the\ SWI}$, which yields values of $-2.96 \pm 0.21‰$ for CB and $-2.05 \pm 1.04‰$ for KHB, indicating that the signature is probably dominated by high-flux sites rather than low-flux sites.

An experimental study by Welch et al. (2003) showed that the oxidation of aqueous ferrous and ferric phases at the SWI and the subsequent precipitation as $Fe(III)_s$ incorporates heavier isotopes in the solid phase $Fe(III)_s$, resulting in a light pore-water dFe value during equilibrium isotope fractionation (Welch et al., 2003). Although this may not be generally applicable under natural conditions, it can be observed in our study area at CBE_{Prox1a} where a lighter pore-water $\delta^{56}Fe_{aq}$ signature is observed at 1.5 cm with $-3.09 \pm 0.14‰$ (ferruginous-manganous zone). In the BW at the same site, we measured an even lighter $\delta^{56}Fe_{aq}$ signature of $-3.94 \pm 0.14‰$ (oxygenated BW). This suggests that the shallower OPD at this site, combined with the high reactive Fe content that minimizes loss during oxidative precipitation, facilitates the preservation of the lighter pore-water $\delta^{56}Fe_{aq}$ signature produced by microbial Fe reduction under these conditions. Although we did not measure the BW $\delta^{56}Fe_{aq}$ signature at the other sites, we cannot rule out that the signature released into the BW might be heavier compared to CBE_{Prox1a}. However, when dFe reaches the oxic and nitrate-containing zone, it could be either stabilized by organic matter as Fe(II) (Jones et al., 2025), or it may be subsequently oxidized to Fe(III) by nitrate and oxygen (Aller, 1994), predominantly in the colloidal size spectrum (Homoky et al., 2021; Staubwasser et al., 2013). A recent study further suggests that benthic $\delta^{56}Fe$ fractionation across the SWI may be limited and the $\delta^{56}Fe_{aq}$ values are subsequently modified by kinetic effects, mixing, or loss in the water column (Hunt et al., 2022). Other studies suggest that Fe oxidation and subsequent precipitation across redox gradients can generate heavier $\delta^{56}Fe_{aq}$ values, either through equilibrium or kinetic isotope effects during oxidation and removal (Ellwood et al., 2019; John et al., 2012; Staubwasser et al., 2013). Homoky et al. (2021) modeled steady-state pore-water Fe production and consumption to decipher whether crustal $\delta^{56}Fe$ signatures were derived from re-precipitation or dissolution and found that dissolution sets the pore-water $\delta^{56}Fe_{aq}$ signal with a minor contribution from Fe precipitation accompanied by a positive fractionation factor consistent with other studies (Staubwasser et al., 2013). Staubwasser et al. (2013) concluded that rapid re-oxidation under alkaline conditions of dFe is slowed down or inhibited because stable Fe carbonate complexes must first dissociate before oxidation can proceed (King, 1998; Pham & Waite, 2008), highlighting the importance of Fe kinetics (Staubwasser et al., 2013). Overall, these observations indicate that multiple mechanisms and not only one dominant is responsible for the $\delta^{56}Fe$ fractionation across the ferruginous to oxic-nitrogenous redox boundary.

In order to use $\delta^{56}Fe$ in seawater as a "semi-quantitative" fingerprint for benthic efflux, it remains to be clarified whether an additional Fe isotope fractionation occurs within the 'biological recycling loop' on the shelf (Schlosser et al., 2018), which is currently unknown. These findings of different possible mechanisms highlight the complexity of Fe isotope systematics in redox transition zones (Staubwasser et al., 2013) and underscore the importance of studying benthic Fe fluxes across different geographic settings more closely to improve global models (Dale et al., 2015; Liu et al., 2025; Tagliabue et al., 2009).

5. Conclusions

In this study, we elaborated the depositional regime and geochemical conditions in two fjords of South Georgia to identify the primary drivers of benthic Fe fluxes. Our findings highlight the importance of considering both abiotic and biotic processes in fjord and shelf sediments when evaluating the magnitude of benthic Fe fluxes and their link to the pore-water $\delta^{56}Fe_{aq}$ at the sediment surface. The pore-water $\delta^{56}Fe_{aq}$ signal shows potential as a

proxy for tracing dFe diffusion into the water column, particularly in settings with high benthic fluxes and narrow oxic zones that preserve the light isotopic signature of reductive processes. Although this signature may be modified by re-oxidation and precipitation near the SWI, sites with higher benthic Fe fluxes and less variable pore-water $\delta^{56}Fe_{aq}$ signatures offer better traceability. In sub-polar and probably many other environments, pore-water $\delta^{56}Fe_{aq}$ fractionation is influenced by the depth of oxygen penetration, the initial composition of Fe (oxyhydr)oxides, reaction kinetics, and the depositional regime, as trough systems act as depocenters for recycled material that alter the initial conditions for fractionation. While the pore-water $\delta^{56}Fe_{aq}$ reflects complex diagenetic processes, it can still provide valuable insights into benthic Fe fluxes if the transformation processes at the SWI are well constrained. To confirm these interpretations, bottom water $\delta^{56}Fe$ measurements are crucial, even though linking the pore-water $\delta^{56}Fe_{aq}$ signature to that of the overlying water column remains challenging. Further detailed studies are needed to resolve the re-oxidation processes within the oxic-nitrate containing zone, probably altering the pore-water $\delta^{56}Fe_{aq}$ signature that characterizes Fe fluxes into the bottom water. Nonetheless, we are cautiously optimistic about the potential of the pore-water $\delta^{56}Fe_{aq}$ 'fingerprint' in surface sediments as an indicator for diffusive dFe into the BW at sites with comparatively high benthic Fe fluxes.

Conflict of Interest

The authors declare no conflicts of interest relevant to this study.

Availability Statement

The data presented in this study are available in the World Data Center PANGAEA via https://doi.org/10.1594/PANGAEA.986658 (Ebner et al., 2025).

Acknowledgments

We thank the captain and crew of RV Polarstern during expedition PS133/2 (Grant AWI_PS133/2_03 & AWI_PS133/2_05). We thank I. Dohrmann (AWI, Bremerhaven), M. Leusch (University of Bremen) and C. Nadolsky (AWI) for their support on board during the sampling campaign. We thank I. Stimac (AWI) for the support in the laboratory during the ^{210}Pb analysis. We thank B. Liu (AWI) for his helpful input on iron flux calculations. We are grateful to R. Middag (NIOZ, Texel) and K. Streuff (MARUM, Bremen) for their valuable input during data discussions. We also want to thank M. Römer (MARUM) for sharing her expertise on methane seepage in South Georgia. We thank E. Miramontes and B. Kockisch (University of Bremen) for the TOC measurements. This work was funded by the AWI INSPIRES III program under the framework of the Helmholtz Research Program "Changing Earth–Sustaining our Future" (PoF IV: Coastal Zones at a Time of Global Change) and the German Research Foundation (DFG 490822598 to KLM). All figures were created using QGIS (Version 3.26.2-Buenos Aires), Grapher Golden Software (Version 20.2.321) and CorelDRAW Graphics Suite 2022. The statistical analysis was conducted using RStudio (Version 2024.12.0) as an interface. We thank the editor Zanna Chase, the associate editor, one anonymous reviewer and Tim Conway for their helpful and constructive comments and suggestions. Open Access funding enabled and organized by Projekt DEAL.

References

Aller, R. C. (1994). Bioturbation and remineralization of sedimentary organic matter: Effects of redox oscillation. *Chemical Geology*, *114*(3–4), 331–345. https://doi.org/10.1016/0009-2541(94)90062-0

Appleby, P. G. (1998). Dating recent sediments by 210Pb: Problems and solutions, seminar on dating of sediments and determination of sedimentation rate (pp. 7–24).

Appleby, P. G., & Oldfield, F. (1978). The calculation of lead-210 dates assuming a constant rate of supply of unsupported 210Pb to the sediment. *Catena*, *5*, 1–8. https://doi.org/10.1016/S0341-8162(78)80002-2

Arias-Ortiz, A., Masqué, P., Garcia-Orellana, J., Serrano, O., Mazarrasa, I., Marbà, N., et al. (2018). Reviews and syntheses: 210Pb-derived sediment and carbon accumulation rates in vegetated coastal ecosystems - Setting the record straight. *Biogeosciences*, *15*(22), 6791–6818. https://doi.org/10.5194/bg-15-6791-2018

Baloza, M., Henkel, S., Geibert, W., Kasten, S., & Holtappels, M. (2022). Benthic carbon remineralization and iron cycling in relation to sea ice cover along the eastern Continental shelf of the antarctic peninsula. *Journal of Geophysical Research: Oceans*, *127*(7), e2021JC018401. https://doi.org/10.1029/2021JC018401

Baloza, M., Henkel, S., Kasten, S., Holtappels, M., & Molari, M. (2023). The impact of sea ice cover on microbial communities in antarctic shelf sediments. *Microorganisms*, *11*(6), 1572. https://doi.org/10.3390/microorganisms11061572

Beard, B. L., & Johnson, C. M. (2004). Fe isotope variations in the modern and ancient Earth and other planetary bodies. *Reviews in Mineralogy and Geochemistry*, *55*(1), 319–357. https://doi.org/10.2138/gsrmg.55.1.319

Beard, B. L., Johnson, C. M., Von Damm, K. L., & Poulson, R. L. (2003). Iron isotope constraints on Fe cycling and mass balance in oxygenated Earth oceans. *Geology*, *31*(7), 629. https://doi.org/10.1130/0091-7613(2003)031<0629:IICOFC>2.0.CO;2

Behrenfeld, M. J., & Falkowski, P. G. (1997). Photosynthetic rates derived from satellite-based chlorophyll concentration. *Limnology & Oceanography*, *42*(1), 1–20. https://doi.org/10.4319/lo.1997.42.1.0001

Bentley, M., Evans, D., Fogwill, C., Hansom, J., Sugden, D., & Kubik, P. (2007). Glacial geomorphology and chronology of deglaciation, south Georgia, sub-antarctic. *Quaternary Science Reviews*, *26*(5–6), 644–677. https://doi.org/10.1016/j.quascirev.2006.11.019

Ben-Yaakov, S. (1973). pH buffering of pore waters of recent anoxic marine sediments. *Limnology & Oceanography*, *18*(1), 86–94. https://doi.org/10.4319/lo.1973.18.1.0086

Berg, S., Jivcov, S., Kusch, S., Kuhn, G., White, D., Bohrmann, G., et al. (2021). Increased petrogenic and biospheric organic carbon burial in subantarctic fjord sediments in response to recent glacier retreat. *Limnology & Oceanography*, *66*(12), 4347–4362. https://doi.org/10.1002/lno.11965

Bianchi, T. S., Arndt, S., Austin, W. E. N., Benn, D. I., Bertrand, S., Cui, X., et al. (2020). Fjords as aquatic critical zones (ACZs). *Earth-Science Reviews*, *203*, 103145. https://doi.org/10.1016/j.earscirev.2020.103145

Biscaye, P. E., & Eittreim, S. L. (1977). Suspended particulate loads and transports in the nepheloid layer of the abyssal Atlantic Ocean. *Marine Geology*, *23*(1–2), 155–172. https://doi.org/10.1016/0025-3227(77)90087-1

Blain, S., Quéguiner, B., Armand, L., Belviso, S., Bombled, B., Bopp, L., et al. (2007). Effect of natural iron fertilization on carbon sequestration in the Southern Ocean. *Nature*, *446*(7139), 1070–1074. https://doi.org/10.1038/nature05700

Bohrmann, G. (2013). *The expedition of the research vessel Polarstern to the Antarctic in 2013 (ANT-XXIX/4)* (p. 169). Alfred-Wegener-Institute for Polar and Marine Research. https://doi.org/10.2312/BzPM_0668_2013

Boldt, K. V., Nittrouer, C. A., Hallet, B., Koppes, M. N., Forrest, B. K., Wellner, J. S., & Anderson, J. B. (2013). Modern rates of glacial sediment accumulation along a 15°S-N transect in fjords from the Antarctic Peninsula to southern Chile. *Journal of Geophysical Research: Earth Surface*, *118*(4), 2072–2088. https://doi.org/10.1002/jgrf.20145

Borrione, I., & Schlitzer, R. (2013). Distribution and recurrence of phytoplankton blooms around South Georgia, Southern Ocean. *Biogeosciences*, *10*(1), 217–231. https://doi.org/10.5194/bg-10-217-2013

Boudreau, B. P. (1997). *Diagenetic models and their implementation: Modelling transport and reactions in aquatic sediments*. Springer Berlin Heidelberg.

Boudreau, B. P., & Scott, M. R. (1978). A model for the diffusion-controlled growth of deep-sea manganese nodules. *American Journal of Science*, *278*(7), 903–929. https://doi.org/10.2475/ajs.278.7.903

Boyd, P. W., & Ellwood, M. J. (2010). The biogeochemical cycle of iron in the ocean. *Nature Geoscience*, *3*(10), 675–682. https://doi.org/10.1038/ngeo964

Breitzke, M. (2006). Physical properties of marine sediments. In H. D. Schulz & M. Zabel (Eds.), *Marine geochemistry* (2nd ed., pp. 28–69). Springer. https://doi.org/10.1007/3-540-32144-6_7

Bullen, T. D., White, A. F., Childs, C. W., Vivit, D. V., & Schulz, M. S. (2001). Demonstration of significant abiotic iron isotope fractionation in nature. *Geology*, *29*(8), 699. https://doi.org/10.1130/0091-7613(2001)029<0699:DOSAII>2.0.CO;2

Burdige, D. J. (2007). Preservation of organic matter in marine sediments: Controls, mechanisms, and an imbalance in sediment organic carbon budgets? *Chemical Reviews*, *107*(2), 467–485. https://doi.org/10.1021/cr050347q

Burdige, D. J., & Komada, T. (2020). Iron redox cycling, sediment resuspension and the role of sediments in low oxygen environments as sources of iron to the water column. *Marine Chemistry*, *223*, 103793. https://doi.org/10.1016/j.marchem.2020.103793

Burnett, W. C., Bokuniewicz, H., Huettel, M., Moore, W. S., & Taniguchi, M. (2003). Groundwater and pore water inputs to the coastal zone. *Biogeochemistry*, *66*(1/2), 3–33. https://doi.org/10.1023/B:BIOG.0000006066.21240.53

Butler, I. B., Archer, C., Vance, D., Oldroyd, A., & Rickard, D. (2005). Fe isotope fractionation on FeS formation in ambient aqueous solution. *Earth and Planetary Science Letters*, *236*(1–2), 430–442. https://doi.org/10.1016/j.epsl.2005.05.022

Canfield, D. E. (1994). Factors influencing organic carbon preservation in marine sediments. *Chemical Geology*, *114*(3–4), 315–329. https://doi.org/10.1016/0009-2541(94)90061-2

Canfield, D. E., & Thamdrup, B. (2009). Towards a consistent classification scheme for geochemical environments, or, why we wish the term 'suboxic' would go away. *Geobiology*, *7*(4), 385–392. https://doi.org/10.1111/j.1472-4669.2009.00214.x

Cline, J. D. (1969). Spectrophotometric determination of hydrogen sulfide in natural waters. *Limnology & Oceanography*, *14*(3), 454–458. https://doi.org/10.4319/lo.1969.14.3.0454

Conway, T. M., & John, S. G. (2014). Quantification of dissolved iron sources to the North Atlantic Ocean. *Nature*, *511*(7508), 212–215. https://doi.org/10.1038/nature13482

Craddock, P. R., & Dauphas, N. (2011). Iron isotopic compositions of geological reference materials and chondrites. *Geostandards and Geoanalytical Research*, *35*(1), 101–123. https://doi.org/10.1111/j.1751-908X.2010.00085.x

Crosby, H. A., Roden, E. E., Johnson, C. M., & Beard, B. L. (2007). The mechanisms of iron isotope fractionation produced during dissimilatory Fe(III) reduction by Shewanella putrefaciens and Geobacter sulfurreducens. *Geobiology*, *5*(2), 169–189. https://doi.org/10.1111/j.1472-4669.2007.00103.x

Curtis, M. L. (2011). *Geological Map of South Georgia (1:250 000 scale). BAS GEOMAP 2 Series, Sheet 4*. British Antarctic Survey.

Dale, A. W., Nickelsen, L., Scholz, F., Hensen, C., Oschlies, A., & Wallmann, K. (2015). A revised global estimate of dissolved iron fluxes from marine sediments: Global Benthic Iron Fluxes. *Global Biogeochemical Cycles*, *29*(5), 691–707. https://doi.org/10.1002/2014GB005017

Death, R., Wadham, J. L., Monteiro, F., Le Brocq, A. M., Tranter, M., Ridgwell, A., et al. (2014). Antarctic ice sheet fertilises the Southern Ocean. *Biogeosciences*, *11*(10), 2635–2643. https://doi.org/10.5194/bg-11-2635-2014

Dickson, A. (2010). Standards for ocean measurements. *Oceanography*, *23*(3), 34–47. https://doi.org/10.5670/oceanog.2010.22

Dorschel, B., Hehemann, L., Viquerat, S., Warnke, F., Dreutter, S., Tenberge, Y. S., et al. (2022). The international bathymetric chart of the Southern Ocean version 2. *Scientific Data*, *9*(1), 275. https://doi.org/10.1038/s41597-022-01366-7

Ebner, B., Henkel, S., Kraal, P., Müller, D., Köster, M., Staubwasser, M., et al. (2025). Solid phase data of surface sediments retrieved from two fjords in South Georgia, sub-Antarctica [Dataset]. *PANGAEA*. https://doi.org/10.1594/PANGAEA.986661

Ellwood, M. J., Hassler, C., Moisset, S., Pascal, L., Danza, F., Peduzzi, S., et al. (2019). Iron isotope transformations in the meromictic Lake Cadagno. *Geochimica et Cosmochimica Acta*, *255*, 205–221. https://doi.org/10.1016/j.gca.2019.04.007

Elrod, V. A., Berelson, W. M., Coale, K. H., & Johnson, K. S. (2004). The flux of iron from continental shelf sediments: A missing source for global budgets. *Geophysical Research Letters*, *31*(12), 2004GL020216. https://doi.org/10.1029/2004GL020216

Farías-Barahona, D., Sommer, C., Sauter, T., Bannister, D., Seehaus, T. C., Malz, P., et al. (2020). Detailed quantification of glacier elevation and mass changes in South Georgia. *Environmental Research Letters*, *15*(3), 034036. https://doi.org/10.1088/1748-9326/ab6b32

Fitzsimmons, J. N., & Conway, T. M. (2023). Novel insights into marine iron biogeochemistry from iron isotopes. *Annual Review of Marine Science*, *15*(1), 383–406. https://doi.org/10.1146/annurev-marine-032822-103431

Freitas, F. S., Pika, P. A., Kasten, S., Jørgensen, B. B., Rassmann, J., Rabouille, C., et al. (2021). New insights into large-scale trends of apparent organic matter reactivity in marine sediments and patterns of benthic carbon transformation. *Biogeosciences*, *18*(15), 4651–4679. https://doi.org/10.5194/bg-18-4651-2021

Froelich, P. N., Klinkhammer, G. P., Bender, M. L., Luedtke, N. A., Heath, G. R., Cullen, D., et al. (1979). Early oxidation of organic matter in pelagic sediments of the eastern equatorial Atlantic: Suboxic diagenesis. *Geochimica et Cosmochimica Acta*, *43*(7), 1075–1090. https://doi.org/10.1016/0016-7037(79)90095-4

Gattuso, J. P., Epitalon, J. M., Lavigne, H., & Orr, J. (2021). Seacarb: Seawater carbonate chemistry. *R package version*, *3.3.0*. http://CRAN.R-project.org/package=seacarb

Geprägs, P., Torres, M. E., Mau, S., Kasten, S., Römer, M., & Bohrmann, G. (2016). Carbon cycling fed by methane seepage at the shallow Cumberland Bay, South Georgia, sub-Antarctic: Methane Seepage in Cumberland Bay. *Geochemistry, Geophysics, Geosystems*, *17*(4), 1401–1418. https://doi.org/10.1002/2016GC006276

Godoy, J. M., Massone, C. G., Carreira, R. S., Wagener, A. R., & Carvalho, F. (2024). Alternatives to 137Cs for 210Pb dating validation in South America and in the Caribbean region: Point and diffuse sources. *Journal of Environmental Radioactivity*, *278*, 107489. https://doi.org/10.1016/j.jenvrad.2024.107489

Gordon, J. E., Haynes, V. M., & Hubbard, A. (2008). Recent glacier changes and climate trends on South Georgia. *Global and Planetary Change*, *60*(1–2), 72–84. https://doi.org/10.1016/j.gloplacha.2006.07.037

Grasshoff, K., Kremlingl, K., & Ehrhardt, M. (1999). *Methods of seawater analysis, third, completely revised and extended edition*. Wiley VCH.

Haeckel, M., Boudreau, B. P., & Wallmann, K. (2007). Bubble-induced porewater mixing: A 3-D model for deep porewater irrigation. *Geochimica et Cosmochimica Acta*, *71*(21), 5135–5154. https://doi.org/10.1016/j.gca.2007.08.011

Henkel, S., Kasten, S., Hartmann, J. F., Silva-Busso, A., & Staubwasser, M. (2018). Iron cycling and stable Fe isotope fractionation in Antarctic shelf sediments, King George Islandl. *Geochimica et Cosmochimica Acta*, *237*, 320–338. https://doi.org/10.1016/j.gca.2018.06.042

Henkel, S., Kasten, S., Poulton, S. W., & Staubwasser, M. (2016). Determination of the stable iron isotopic composition of sequentially leached iron phases in marine sediments. *Chemical Geology*, *421*, 93–102. https://doi.org/10.1016/j.chemgeo.2015.12.003

Henkel, S., Liu, B., Staubwasser, M., Kasemann, S. A., Meixner, A., Aromokeye, D., et al. (2025). Stable iron isotope signals indicate a pseudo-abiotic process driving deep iron release in methanic sediments. *Biogeosciences*, *22*, 1673–1696. https://doi.org/10.5194/bg-22-1673-2025

Herbert, L. C., Zhu, Q., Michaud, A. B., Laufer-Meiser, K., Jones, C. K., Riedinger, N., et al. (2021). Benthic iron flux influenced by climate-sensitive interplay between organic carbon availability and sedimentation rate in Arctic fjords. *Limnology & Oceanography*, *66*(9), 3374–3392. https://doi.org/10.1002/lno.11885

Heron, G., Crouzet, C., Bourg, A. C. M., & Christensen, T. H. (1994). Speciation of Fe(II) and Fe(III) in contaminated aquifer sediments using chemical extraction techniques. *Environmental Science & Technology*, *28*(9), 1698–1705. https://doi.org/10.1021/es00058a023

Hodgson, D. A., Graham, A. G. C., Griffiths, H. J., Roberts, S. J., Cofaigh, C. Ó., Bentley, M. J., & Evans, D. J. A. (2014). Glacial history of sub-Antarctic South Georgia based on the submarine geomorphology of its fjords. *Quaternary Science Reviews*, *89*, 129–147. https://doi.org/10.1016/j.quascirev.2013.12.005

Homoky, W. B., Conway, T. M., John, S. G., König, D., Deng, F., Tagliabue, A., & Mills, R. A. (2021). Iron colloids dominate sedimentary supply to the ocean interior. *Proceedings of the National Academy of Sciences*, *118*(13), e2016078118. https://doi.org/10.1073/pnas.2016078118

Homoky, W. B., John, S. G., Conway, T. M., & Mills, R. A. (2013). Distinct iron isotopic signatures and supply from marine sediment dissolution. *Nature Communications*, *4*(1), 2143. https://doi.org/10.1038/ncomms3143

Hunt, H. R., Summers, B. A., Sieber, M., Krisch, S., Al-Hashem, A., Hopwood, M., et al. (2022). Distinguishing the influence of sediments, the Congo River, and water-mass mixing on the distribution of iron and its isotopes in the Southeast Atlantic Ocean. *Marine Chemistry*, *247*, 104181. https://doi.org/10.1016/j.marchem.2022.104181

Jickells, T. D., An, Z. S., Andersen, K. K., Baker, A. R., Bergametti, G., Brooks, N., et al. (2005). Global iron connections between desert dust, ocean biogeochemistry, and climate. *Science*, *308*(5718), 67–71. https://doi.org/10.1126/science.1105959

John, S. G., Helgoe, J., Townsend, E., Weber, T., DeVries, T., Tagliabue, A., et al. (2018). Biogeochemical cycling of Fe and Fe stable isotopes in the Eastern Tropical South Pacific. *Marine Chemistry*, *201*, 66–76. https://doi.org/10.1016/j.marchem.2017.06.003

John, S. G., Mendez, J., Moffett, J., & Adkins, J. (2012). The flux of iron and iron isotopes from San Pedro Basin sediments. *Geochimica et Cosmochimica Acta*, *93*, 14–29. https://doi.org/10.1016/j.gca.2012.06.003

Johnson, C. M., & Beard, B. L. (2005). Biogeochemical cycling of iron isotopes. *Science*, *309*(5737), 1025–1027. https://doi.org/10.1126/science.1112552

Jones, R. L., Hawkings, J. R., Meredith, M. P., Lohan, M. C., Moore, O. W., Sherrell, R. M., et al. (2025). Antarctic glaciers export carbon-stabilised iron(II)-rich particles to the surface Southern Ocean. *Nature Communications*, *16*(1), 5015. https://doi.org/10.1038/s41467-025-59981-y

Jørgensen, B., Glud, R., & Holby, O. (2005). Oxygen distribution and bioirrigation in Arctic fjord sediments (Svalbard, Barents Sea). *Marine Ecology Progress Series*, *292*, 85–95. https://doi.org/10.3354/meps292085

Jørgensen, B. B. (1978). A comparison of methods for the quantification of bacterial sulfate reduction in coastal marine sediments: II. Calculation from mathematical models. *Geomicrobiology Journal*, *1*, 29–47. https://doi.org/10.1080/01490457809377722

Jørgensen, B. B. (2021). Sulfur biogeochemical cycle of marine sediments. *Geochem. Perspect.*, *10*, 145–307. https://doi.org/10.7185/geochemperspr.10.2

Jørgensen, B. B., & Kasten, S. (2006). Sulfur cycling and methane oxidation. In *Marine geochemistry* (pp. 271–309). Springer-Verlag. https://doi.org/10.1007/3-540-32144-6_8

Kallmeyer, J., Ferdelman, T. G., Weber, A., Fossing, H., & Jørgensen, B. B. (2004). A cold chromium distillation procedure for radiolabeled sulfide applied to sulfate reduction measurements. *Limnology and Oceanography: Methods*, *2*(6), 171–180. https://doi.org/10.4319/lom.2004.2.171

Kasten, S. (2023). The expedition PS133/2 of the research vessel Polarstern to the Scotia Sea in 2022. *Berichte zur Polar- und Meeresforschung, Bremerhaven, Alfred-Wegener-Institut Helmholtz-Zentrum für Polar- und Meeresforschung*, *775*, 183. https://doi.org/10.57738/BzPM_0775_2023

King, D. W. (1998). Role of carbonate speciation on the oxidation rate of Fe(II) in aquatic systems. *Environmental Science & Technology*, *32*(19), 2997–3003. https://doi.org/10.1021/es980206o

Klar, J. K., Homoky, W. B., Statham, P. J., Birchill, A. J., Harris, E. L., Woodward, E. M. S., et al. (2017). Stability of dissolved and soluble Fe(II) in shelf sediment pore waters and release to an oxic water column. *Biogeochemistry*, *135*(1–2), 49–67. https://doi.org/10.1007/s10533-017-0309-x

Klar, J. K., James, R. H., Gibbs, D., Lough, A., Parkinson, I., Milton, J. A., et al. (2017). Isotopic signature of dissolved iron delivered to the Southern Ocean from hydrothermal vents in the East Scotia Sea. *Geology*, *45*(4), 351–354. https://doi.org/10.1130/G38432.1

Köster, M., Staubwasser, M., Meixner, A., Kasemann, S. A., Manners, H. R., Morono, Y., et al. (2023). Uniquely low stable iron isotopic signatures in deep marine sediments caused by Rayleigh distillation. *Scientific Reports*, *13*(1), 10281. https://doi.org/10.1038/s41598-023-37254-2

Kraal, P., Van Genuchten, C. M., & Behrends, T. (2022). Phosphate coprecipitation affects reactivity of iron (oxyhydr)oxides towards dissolved iron and sulfide. *Geochimica et Cosmochimica Acta*, *321*, 311–328. https://doi.org/10.1016/j.gca.2021.12.032

Krishnaswamy, S., Lal, D., Martin, J. M., & Meybeck, M. (1971). Geochronology of lake sediments. *Earth and Planetary Science Letters*, *11*(1–5), 407–414. https://doi.org/10.1016/0012-821X(71)90202-0

Küster, F. W., & Thiel, A. (1985). *Rechentafeln für die chemische Analytik* (103rd ed.). De Gruyter. https://doi.org/10.1515/9783111666464

Lacan, F., Radic, A., Jeandel, C., Poitrasson, F., Sarthou, G., Pradoux, C., & Freydier, R. (2008). Measurement of the isotopic composition of dissolved iron in the open ocean. *Geophysical Research Letters*, *35*(24), L24610. https://doi.org/10.1029/2008GL035841

Laufer, K., Michaud, A. B., Røy, H., & Jørgensen, B. B. (2020). Reactivity of iron minerals in the seabed toward microbial reduction – A comparison of different extraction techniques. *Geomicrobiology Journal*, *37*(2), 170–189. https://doi.org/10.1080/01490451.2019.1679291

Laufer-Meiser, K., Michaud, A. B., Maisch, M., Byrne, J. M., Kappler, A., Patterson, M. O., et al. (2021). Potentially bioavailable iron produced through benthic cycling in glaciated Arctic fjords of Svalbard. *Nature Communications*, *12*(1), 1349. https://doi.org/10.1038/s41467-021-21558-w

Lenstra, W. K., Hermans, M., Sèguret, M. J. M., Witbaard, R., Severmann, S., Behrends, T., & Slomp, C. P. (2021). Coastal hypoxia and eutrophication as key controls on benthic release and water column dynamics of iron and manganese. *Limnol. and Oceangr.*, *66*(3), 807–826. https://doi.org/10.1002/lno.11644

Lešić, N.-M., Streuff, K. T., Bohrmann, G., Kasten, S., & Kuhn, G. (2024). Spatial and temporal variability in Holocene trough-fill sediments, King Haakon trough system, sub-Antarctic South Georgia. *Quat. Sci. Adv.*, *13*, 100156. https://doi.org/10.1016/j.qsa.2023.100156

Liu, T., Plass, A., Gledhill, M., Scholz, F., Achterberg, E. P., & Hopwood, M. J. (2025). Trace metal effluxes from Peruvian shelf sediments constrained in parallel by benthic lander mounted pumps and pelagic rosette sampling. *Journal of Geophysical Research: Biogeosciences*, *130*(5), e2024JG008583. https://doi.org/10.1029/2024JG008583

Mair, B. F. (1981). Geological observations in the moraine Fjord area, south Georgia. *British Antarctic Survey Bulletin*, *53*, 11–19.

Matano, R. P., Combes, V., Young, E. F., & Meredith, M. P. (2020). Modeling the impact of ocean circulation on chlorophyll blooms around south Georgia, Southern Ocean. *Journal of Geophysical Research: Oceans*, *125*, 9. https://doi.org/10.1029/2020JC016391

McAnena, A., Severmann, S., Guilbaud, R., & Poulton, S. W. (2024). Iron isotope fractionation during sulfide-promoted reductive dissolution of iron (oxyhydr)oxide minerals. *Geochimica et Cosmochimica Acta*, *369*, 17–34. https://doi.org/10.1016/j.gca.2024.01.032

Menard, H. W., & Smith, S. M. (1966). Hypsometry od ocean basin provinces. *Journal of Geophysical Research*, *71*, 18.

Meredith, M. P., Watkins, J. L., Murphy, E. J., Ward, P., Bone, D. G., Thorpe, S. E., et al. (2003). Southern ACC front to the northeast of South Georgia: Pathways, characteristics, and fluxes. *Journal of Geophysical Research*, *108*(C5), 2001JC001227. https://doi.org/10.1029/2001JC001227

Michaud, A. B., Laufer, K., Findlay, A., Pellerin, A., Antler, G., Turchyn, A. V., et al. (2020). Glacial influence on the iron and sulfur cycles in Arctic fjord sediments (Svalbard). *Geochimica et Cosmochimica Acta*, *280*, 423–440. https://doi.org/10.1016/j.gca.2019.12.033

Millero, F. J. (2001). *The physical chemistry of natural waters*. Wiley Interscience.

Millero, J., & Izaguirre, M. (1986). The oxidation kinetics of Fe(II) in seawater. *Geochimica et Cosmochimica Acta*, *51*, 793–801. https://doi.org/10.1016/0016-7037(87)90093-7

Mole, R., von Appen, W. J., Becker, H., Haumann, F. A., Kanzow, T., Pinango, A., et al. (2025). Wind-driven iron supply by Ekman Buoyancy flux enhances phytoplankton bloom in the Antarctic circumpolar current. *Journal of Geophysical Research: Oceans*, *130*(8), e2025JC022530. https://doi.org/10.1029/2025JC022530

Monien, D., Monien, P., Brünjes, R., Widmer, T., Kappenberg, A., Silva Busso, A. A., et al. (2017). Meltwater as a source of potentially bioavailable iron to Antarctica waters. *Antarctic Science*, *29*(3), 277–291. https://doi.org/10.1017/S095410201600064X

Monien, P., Lettmann, K. A., Monien, D., Asendorf, S., Wölfl, A. C., Lim, C. H., et al. (2014). Redox conditions and trace metal cycling in coastal sediments from the maritime Antarctic. *Geochimica et Cosmochimica Acta*, *141*, 26–44. https://doi.org/10.1016/j.gca.2014.06.003

Müller, D., Liu, B., Geibert, W., Holtappels, M., Sander, L., Miramontes, E., et al. (2025). Depositional controls and budget of organic carbon burial in fine-grained sediments of the North Sea – The Helgoland Mud Area as a natural laboratory. *Biogeosciences*, *22*(11), 2541–2567. https://doi.org/10.5194/bg-22-2541-2025

Müller, D., Liu, B., Holtappels, M., Geibert, W., Henkel, S., & Kasten, S. (2026). Rates and pathways of organic matter remineralisation in different sedimentary environments of the Helgoland Mud Area, North Sea. *Continental Shelf Research*, *298*, 105632. https://doi.org/10.1016/j.csr.2025.105632

Nielsdóttir, M. C., Bibby, T. S., Moore, C. M., Hinz, D. J., Sanders, R., Whitehouse, M., et al. (2012). Seasonal and spatial dynamics of iron availability in the Scotia Sea. *Marine Chemistry*, *130–131*, 62–72. https://doi.org/10.1016/j.marchem.2011.12.004

Orsi, A. H., Whitworth, T., & Nowlin, W. D. (1995). On the meridional extent and fronts of the Antarctic Circumpolar Current. *Deep-Sea Research Part A Oceanographic Research Papers*, *42*(5), 641–673. https://doi.org/10.1016/0967-0637(95)00021-W

Pham, A. N., & Waite, T. D. (2008). Oxygenation of Fe(II) in natural waters revisited: Kinetic modeling approaches, rate constant estimation and the importance of various reaction pathways. *Geochimica et Cosmochimica Acta*, *72*(15), 3616–3630. https://doi.org/10.1016/j.gca.2008.05.032

Pham, M. K., Sanchez-Cabeza, J. A., Povinec, P. P., Andor, K., Arnold, D., Benmansour, M., et al. (2008). A new Certified reference material for radionuclides in Irish sea sediment (IAEA-385). *Applied Radiation and Isotopes*, *66*(11), 1711–1717. https://doi.org/10.1016/j.apradiso.2007.10.020

Radic, A., Lacan, F., & Murray, J. W. (2011). Iron isotopes in the seawater of the equatorial Pacific Ocean: New constraints for the oceanic iron cycle. *Earth and Planetary Science Letters*, *306*(1–2), 1–10. https://doi.org/10.1016/j.epsl.2011.03.015

Raiswell, R., & Anderson, T. F. (2005). Reactive iron enrichment in sediments deposited beneath euxinic bottom waters: Constraints on supply by shelf recycling. *Geol. Soc. Lond. Spec. Publ.*, *248*(1), 179–194. https://doi.org/10.1144/GSL.SP.2005.248.01.10

Raiswell, R., Tranter, M., Benning, L. G., Siegert, M., Death, R., Huybrechts, P., & Payne, T. (2006). Contributions from glacially derived sediment to the global iron (oxyhydr)oxide cycle: Implications for iron delivery to the oceans. *Geochimica et Cosmochimica Acta*, *70*(11), 2765–2780. https://doi.org/10.1016/j.gca.2005.12.027

Rickard, D. (1997). Kinetics of pyrite formation by the H2S oxidation of iron (II) monosulfide in aqueous solutions between 25 and 125°C: The rate equation. *Geochimica et Cosmochimica Acta*, *61*(1), 115–134. https://doi.org/10.1016/S0016-7037(96)00321-3

Riedinger, N., Formolo, M. J., Lyons, T. W., Henkel, S., Beck, A., & Kasten, S. (2014). An inorganic geochemical argument for coupled anaerobic oxidation of methane and iron reduction in marine sediments. *Geobiology*, *12*(2), 172–181. https://doi.org/10.1111/gbi.12077

Robbins, J. A. (1986). A model for particle-selective transport of tracers in sediments with conveyor belt deposit feeders. *Journal of Geophysical Research*, *91*(C7), 8542–8558. https://doi.org/10.1029/JC091iC07p08542

Römer, M., Torres, M., Kasten, S., Kuhn, G., Graham, A. G. C., Mau, S., et al. (2014). First evidence of widespread active methane seepage in the Southern Ocean, off the sub-antarctic Island of South Georgia. *Earth and Planetary Science Letters*, *403*, 166–177. https://doi.org/10.1016/j.epsl.2014.06.036

Røy, H., Weber, H. S., Tarpgaard, I. H., Ferdelman, T. G., & Jørgensen, B. B. (2014). Determination of dissimilatory sulfate reduction rates in marine sediment via radioactive 35S tracer. *Limnology and Oceanography: Methods*, *12*(4), 196–211. https://doi.org/10.4319/lom.2014.12.196

Roy, R. N., Roy, L. N., Vogel, K. M., Porter-Moore, C., Pearson, T., Good, C. E., et al. (1993). The dissociation constants of carbonic acid in seawater at salinities 5 to 45 and temperatures 0 to 45oC. *Marine Chemistry*, *44*(2–4), 249–267. https://doi.org/10.1016/0304-4203(93)90207-5

Schlosser, C., Schmidt, K., Aquilina, A., Homoky, W. B., Castrillejo, M., Mills, R. A., et al. (2018). Mechanisms of dissolved and labile particulate iron supply to shelf waters and phytoplankton blooms off South Georgia, Southern Ocean. *Biogeosciences*, *15*(16), 4973–4993. https://doi.org/10.5194/bg-15-4973-2018

Schnakenberg, A., Aromokeye, D. A., Kulkarni, A., Maier, L., Wunder, L. C., Richter-Heitmann, T., et al. (2021). Electron acceptor availability shapes anaerobically methane oxidizing archaea (ANME) communities in south Georgia sediments. *Frontiers in Microbiology*, *12*, 617280. https://doi.org/10.3389/fmicb.2021.617280

Schoenberg, R., & Von Blanckenburg, F. (2005). An assessment of the accuracy of stable Fe isotope ratio measurements on samples with organic and inorganic matrices by high-resolution multicollector ICP-MS. *International Journal of Mass Spectrometry*, *242*(2–3), 257–272. https://doi.org/10.1016/j.ijms.2004.11.025

Scholz, F., Severmann, S., McManus, J., Noffke, A., Lomnitz, U., & Hensen, C. (2014). On the isotope composition of reactive iron in marine sediments: Redox shuttle versus early diagenesis. *Chemical Geology*, *389*, 48–59. https://doi.org/10.1016/j.chemgeo.2014.09.009

Seeberg-Elverfeldt, J., Schlüter, M., Feseker, T., & Kölling, M. (2005). Rhizon sampling of porewaters near the sediment-water interface of aquatic systems. *Limnology and Oceanography: Methods*, *3*(8), 361–371. https://doi.org/10.4319/lom.2005.3.361

Severmann, S., McManus, J., Berelson, W. M., & Hammond, D. E. (2010). The continental shelf benthic iron flux and its isotope composition. *Geochimica et Cosmochimica Acta*, *74*(14), 3984–4004. https://doi.org/10.1016/j.gca.2010.04.022

Shapiro, S. S., & Wilk, M. B. (1965). An analysis of variance test for normality (complete samples). *Biometrika*, *52*(3/4), 591–611. https://doi.org/10.2307/2333709

Sieber, M., Conway, T. M., de Souza, G. F., Hassler, C. S., Ellwood, M. J., & Vance, D. (2021). Isotopic fingerprinting of biogeochemical processes and iron sources in the iron-limited surface Southern Ocean. *Earth and Planetary Science Letters*, *567*, 116967. https://doi.org/10.1016/j.epsl.2021.116967

Sivan, O., Adler, M., Pearson, A., Gelman, F., Bar-Or, I., John, S. G., & Eckert, W. (2011). Geochemical evidence for iron-mediated anaerobic oxidation of methane. *Limnology & Oceanography*, *56*(4), 1536–1544. https://doi.org/10.4319/lo.2011.56.4.1536

Smith, S. L. (2018). *Sense of place visualization for the whaling station remains of South Georgia Island*. [Doctoral Thesis] (pp. 163–170). University of Dundee.

Soetaert, K., Hofmann, A. F., Middelburg, J. J., Meysman, F. J. R., & Greenwood, J. (2007). The effect of biogeochemical processes on pH. *Marine Chemistry*, *105*(1–2), 30–51. https://doi.org/10.1016/j.marchem.2006.12.012

Staubwasser, M., Schoenberg, R., von Blanckenburg, F., Krüger, S., & Pohl, C. (2013). Isotope fractionation between dissolved and suspended particulate Fe in the oxic and anoxic water column of the Baltic Sea. *Biogeosciences*, *10*(1), 233–245. https://doi.org/10.5194/bg-10-233-2013

Staubwasser, M., von Blanckenburg, F., & Schoenberg, R. (2006). Iron isotopes in the early marine diagenetic iron cycle. *Geology*, *34*(8), 629. https://doi.org/10.1130/G22647.1

Steinsberger, T., Schmid, M., Wüest, A., Schwefel, R., Wehrli, B., & Müller, B. (2017). Organic carbon mass accumulation rate regulates the flux of reduced substances from the sediments of deep lakes. *Biogeosciences*, *14*(13), 3275–3285. https://doi.org/10.5194/bg-14-3275-2017

Stevenson, E. I., Fantle, M. S., Das, S. B., Williams, H. M., & Aciego, S. M. (2017). The iron isotopic composition of subglacial streams draining the Greenland ice sheet. *Geochimica et Cosmochimica Acta*, *213*, 237–254. https://doi.org/10.1016/j.gca.2017.06.002

Stimpfle, J., Koch, F., Ebner, B., Völkner, C., Zitoun, R., Sukekava, C., et al. (2026). Glacially derived iron is more bioavailable to Antarctic phytoplankton than other sources. *Communications Earth & Environment*. https://doi.org/10.1038/s43247-025-03092-5

Stoll, M. H. C., Bakker, K., Nobbe, G. H., & Haese, R. R. (2001). Continuous-Flow analysis of dissolved inorganic carbon content in seawater. *Analytical Chemistry*, *73*(17), 4111–4116. https://doi.org/10.1021/ac010303r

Stookey, L. L. (1970). Ferrozine-a new spectrophotometric reagent for iron. *Analytical Chemistry*, *42*(7), 779–781. https://doi.org/10.1021/ac60289a016

Streuff, K. T., Lešić, N.-M., Kuhn, G., Römer, M., Kasten, S., & Bohrmann, G. (2024). Glacial history of the King Haakon trough system, sub-Antarctic South Georgia. *Quaternary Science Reviews*, *338*, 108749. https://doi.org/10.1016/j.quascirev.2024.108749

Syvitski, J. P. M. (1989). On the deposition of sediment within glacier-influenced fjords: Oceanographic controls. *Marine Geology*, *85*(2–4), 301–329. https://doi.org/10.1016/0025-3227(89)90158-8

Tagliabue, A., Bopp, L., & Aumont, O. (2009). Evaluating the importance of atmospheric and sedimentary iron sources to Southern Ocean biogeochemistry. *Geophysical Research Letters*, *36*(13), 2009GL038914. https://doi.org/10.1029/2009GL038914

Tagliabue, A., Bowie, A. R., DeVries, T., Ellwood, M. J., Landing, W. M., Milne, A., et al. (2019). The interplay between regeneration and scavenging fluxes drives ocean iron cycling. *Nature Communications*, *10*(1), 4960. https://doi.org/10.1038/s41467-019-12775-5

Takeshita, Y., Johnson, K. S., Coletti, L. J., Jannasch, H. W., Walz, P. M., & Warren, J. K. (2020). Assessment of pH dependent errors in spectrophotometric pH measurements of seawater. *Marine Chemistry*, *223*, 103801. https://doi.org/10.1016/j.marchem.2020.103801

Tian, H.-A., Van Manen, M., Bunnell, Z. B., Jung, J., Lee, S. H., Kim, T. W., et al. (2023). Biogeochemistry of iron in coastal Antarctica: Isotopic insights for external sources and biological uptake in the Amundsen Sea polynyas. *Geochimica et Cosmochimica Acta*, *363*, 51–67. https://doi.org/10.1016/j.gca.2023.10.029

Tichit, P., Brickle, P., Newton, R. J., Convey, P., & Dawson, W. (2024). Introduced species infiltrate recent stages of succession after glacial retreat on sub-Antarctic South Georgia. *NeoBiota*, *92*, 85–110. https://doi.org/10.3897/neobiota.92.117226

Tranter, M., & Wadham, J. L. (2014). *Geochemical weathering in glacial and proglacial environments, treatise on geochemistry* (pp. 157–173). Elsevier. https://doi.org/10.1016/B978-0-08-095975-7.00505-2

van de Velde, S. J., Dale, A. W., & Arndt, S. (2023). Bioturbation and the δ^{56} Fe signature of dissolved iron fluxes from marine sediments. *Royal Society Open Science*, *10*(1), 220010. https://doi.org/10.1098/rsos.220010

Wadham, J. L., Death, R., Monteiro, F. M., Tranter, M., Ridgwell, A., Raiswell, R., & Tulaczyk, S. (2013). The potential role of the Antarctic Ice Sheet in global biogeochemical cycles. *Earth and Environmental Science Transactions of the Royal Society of Edinburgh*, *104*(1), 55–67. https://doi.org/10.1017/S1755691013000108

Wadham, J. L., Tranter, M., Skidmore, M., Hodson, A. J., Priscu, J., Lyons, W. B., et al. (2010). Biogeochemical weathering under ice: Size matters: Glacial biogeochemical weathering. *Global Biogeochemical Cycles*, *24*, GB3025. https://doi.org/10.1029/2009GB003688

Wehrmann, L. M., Formolo, M. J., Owens, J. D., Raiswell, R., Ferdelman, T. G., Riedinger, N., & Lyons, T. W. (2014). Iron and manganese speciation and cycling in glacially influenced high-latitude fjord sediments (West Spitsbergen, Svalbard): Evidence for a benthic recycling-transport mechanism. *Geochimica et Cosmochimica Acta*, *141*, 628–655. https://doi.org/10.1016/j.gca.2014.06.007

Wei, B., Müller, D., Kusch, S., Niu, L., Hefter, J., Sander, L., et al. (2025). Twice the global average carbon burial efficiency in the Helgoland Mud Area of the North Sea: Insights into carbon sequestration in small-size depocenters on sand-dominated shelves. *Chemical Geology*, *681*, 122712. https://doi.org/10.1016/j.chemgeo.2025.122712

Welch, S. A., Beard, B. L., Johnson, C. M., & Braterman, P. S. (2003). Kinetic and equilibrium Fe isotope fractionation between aqueous Fe(II) and Fe(III). *Geochimica et Cosmochimica Acta*, *67*(22), 4231–4250. https://doi.org/10.1016/S0016-7037(03)00266-7

Winkler, L. W. (1888). Die Bestimmung des im Wasser gelösten Sauerstoffes. *Berichte Dtsch. Chem. Ges*, *21*(2), 2843–2854. https://doi.org/10.1002/cber.188802102122

Wunder, L. C., Aromokeye, D. A., Yin, X., Richter-Heitmann, T., Willis-Poratti, G., Schnakenberg, A., et al. (2021). Iron and sulfate reduction structure microbial communities in (sub-) antarctic sediments. *ISME Journal*, *15*(12), 3587–3604. https://doi.org/10.1038/s41396-021-01014-9

Xu, S., Liu, B., Arndt, S., Kasten, S., & Wu, Z. (2023). Assessing global-scale organic matter reactivity patterns in marine sediments using a lognormal reactive continuum model. *Biogeosciences*, *20*(12), 2251–2263. https://doi.org/10.5194/bg-20-2251-2023

Zanker, J. C., Young, E., Holland, P. R., Haigh, I. D., & Brickle, P. (2024). Oceanographic variability in Cumberland Bay, south Georgia, and its implications for glacier retreat. *Journal of Geophysical Research: Oceans*, *129*(2), e2023JC020507. https://doi.org/10.1029/2023JC020507

Zhang, R., John, S. G., Zhang, J., Ren, J., Wu, Y., Zhu, Z., et al. (2015). Transport and reaction of iron and iron stable isotopes in glacial meltwaters on Svalbard near Kongsfjorden: From rivers to estuary to ocean. *Earth and Planetary Science Letters*, *424*, 201–211. https://doi.org/10.1016/j.epsl.2015.05.031

Zhao, Y., Moore, O. W., Xiao, K.-Q., Curti, L., Farina, A. O., Banwart, S. A., & Peacock, C. L. (2022). The role and fate of organic carbon during aging of ferrihydrite. *Geochimica et Cosmochimica Acta*, *335*, 339–355. https://doi.org/10.1016/j.gca.2022.07.003

Zhou, Z., Henkel, S., Kasten, S., & Holtappels, M. (2023). The iron redox battery in sandy sediments: Its impact on organic matter remineralization and phosphorus cycling. *Science of the Total Environment*, *865*, 161168. https://doi.org/10.1016/j.scitotenv.2022.161168

Zonneveld, K. A. F., Versteegh, G. J. M., Kasten, S., Eglinton, T. I., Emeis, K.-C., Huguet, C., et al. (2010). Selective preservation of organic matter in marine environments; processes and impact on the sedimentary record. *Biogeosciences*, *7*(2), 483–511. https://doi.org/10.5194/bg-7-483-2010